Appendix-II

Reprints of Published Papers

RSC Advances

PAPER

Cite this: *RSC Adv.*, 2015, **5**, 41780

Submicron ZnO raspberries as effective catalysts for Fries rearrangement

Mohammed Ali, Hasimur Rahaman, Sudip Kumar Pal, Nikita Kar and Sujit Kumar Ghosh*

Received 25th February 2015
Accepted 1st May 2015

DOI: 10.1039/c5ra03448e

www.rsc.org/advances

o-Xylene-in-water emulsion droplets have been exploited as soft templates for the synthesis of submicrometer-sized raspberry-like ZnO morphologies. The optical properties, structure and morphology of the microstructures have been characterised by absorption and fluorescence spectroscopy, Fourier transform infrared spectroscopy, scanning electron microscopy, transmission electron microscopy, energy dispersive X-ray spectroscopy, X-ray diffraction and selected area electron diffraction analysis. It has been found that the microstructures could act as an environmentally benign and cost-effective alternative to conventional Lewis acid catalysts for the illustrious Fries rearrangement of *o*-methylphenyl acetate to 3-methyl-4-hydroxyacetophenone, employed as the model reaction and which has been probed by NMR spectroscopic studies.

1. Introduction

In recent years, self-assembly of nanoscale objects has pioneered a facile strategy to design micrometer-sized hollow structures that have attracted increasing attention because of their specific morphology, fascinating properties and wide applications in physics, chemistry, biology and materials science.[1] Amongst the three different approaches currently explored to effect ordering of nanoparticles by self-assembly processes, liquid–liquid interfaces offer an important alternative scaffold for the organisation of nanoscale substances into higher-order assemblies.[2] Although catalysis is a mature field, it possesses a vital role in chemical-based industries, accounting for about a quarter of the world's gross domestic product.[3] The field of nanocatalysis has undergone an exponential growth during the past decade.[4] This is due to the fact that particles in the nanometer size regime inherently provide a high surface-to-volume ratio, making them attractive candidates for catalysis.[5] The application of transition metal oxides in the nanometer size regime in catalysis has become fascinating because they manipulate the surface activity of the metal and hence, the catalysis at the nanoscale, imparting activity and selectivity to heterogeneous catalysis.[6] The benefit of using heterogeneous catalysis is the facile recovery and recyclability of the catalyst materials and thus, meet the modern requirements for green catalysts.[7] Amongst the transition metal oxides, zinc oxide (ZnO) at the nanoscale dimension have attracted immense interest due to its direct wide band gap (3.37 eV), high exciton binding energy (60 meV) and the opportunity to vary its properties by morphological tuneability provides new chemical insights from an old material.[8] In addition to these physico-chemical properties, numerous environmental advantages, such as, non-toxicity, corrosion resistance, recyclability and easy disposal of the material have encouraged its application as greener catalysts in a diverse range of catalytic and photocatalytic reactions.[8] In the early 1900s, Fries and co-worker reacted phenolic esters of acetic and chloroacetic acid with aluminum chloride and isolated a mixture of *o*- and *p*-acetyl- and chloroacetyl phenols and in general, the conversion of phenolic esters to the corresponding *o*- and/or *p*-substituted phenolic ketones and aldehydes, in the presence of Lewis or Brønsted acids has been recognized as the Fries rearrangement.[9] Different types of Fries rearrangement have been reported so far in the literature using varieties of catalyst materials. For example, Paul and colleague[10] has shown that zinc powder efficiently catalyzes the selective Fries rearrangement of acetylated phenols under microwave heating or with conventional heating in the presence of *N*,*N*-dimethylformamide and in some cases, it was seen that different products were obtained using microwave heating and conventional heating. Krishnamurthy and co-authors[11] reported a convenient way to carry out the Fries rearrangement of phenolic esters to hydroxyphenyl ketones by refluxing in nitrobenzene in the presence of Nafion-H, a solid superacidic resin sulfonic acid catalyst. Belokon and group[12] reported $TiCl_4$-catalysed Fries rearrangement *via* regioselective acylation of *p*-hydroxy [2.2] *para*-cyclophane to *o*-acylhydroxy [2.2] *para*-cyclophanes. Dupont and colleagues[13] have optimized the Fries rearrangement with methanesulfonic acid to give *p*-hydroxyacetophenone with high conversion and selectivity. However, the Fries rearrangement of aryl esters, a special case of Friedel–Craft

Department of Chemistry, Assam University, Silchar-788011, India. E-mail: sujit.kumar.ghosh@aus.ac.in

acylation provides an important route for the synthesis of aromatic hydroxyl aryl ketones which are important intermediates for several pharmaceuticals, such as, paracetamol, salbutamol *etc.* However, the use of aluminium chloride can lead to violations of several principles of green chemistry through the release of hazardous substances in the environment. While the present state-of-the-art literature reveals that ZnO at the bulk or at the nanoscale has been employed as greener catalysts in Friedel–Crafts acylation, Knoevenagel condensation, Biginelli reaction, Hantzsch condensation, phospha-Michael addition, Beckmann rearrangement and so on[14] and Fries rearrangement has been carried out using a wide variety of heterogeneous media or catalysts *viz.*, scandium trifluoromethanesulfonate,[15] sulfated zirconia,[16] zeolite,[17] electron beam irradiation within a cyclodextrin inclusion complex,[18] microwave irradiation,[19] ionic liquids,[20] *etc.*; with the advancement of nanotechnology, therefore, it seems quite appealing to design the landscape of a greener chemical approach for the Fries rearrangement. In this article, we have reported a soft-templated strategy for the synthesis of microstructured zinc oxide assemblies and exploited the particles as viable alternatives to conventional Lewis acid catalysts in the Fries rearrangement of *o*-methylphenyl acetate to 3-methyl-4-hydroxyacetophenone employed as the model reaction.

2. Experimental

2.1. Reagents and instruments

All the reagents used were of analytical reagent grade. Zinc acetate dihydrate [$Zn(OOCCH_3)_2 \cdot 2H_2O$] (Sigma-Aldrich), potassium hydroxide (S. D. Fine Chemicals, India), hydrochloric acid (Qualigens' Fine Chemicals, India) were used as received. *o*-Xylene (Sisco Research Laboratories, India) and were used without further purification. Double distilled water was used throughout the course of the investigation. The temperature was 298 $\pm$ 1 K for all experiments.

Absorption spectrum was recorded in a Lambda-750 digital UV-vis NIR spectrophotometer (PerkinElmer, England) using the solid sample accessories. Fluorescence spectrum was measured with a PerkinElmer LS-45 spectrofluorimeter equipped with a pulsed xenon lamp and a photomultiplier tube with R-928 spectral response. The spectrofluorimeter was linked to a personal computer and utilized the FL WinLab software package for data collection and processing. Scanning electron microscopic (SEM) images were recorded by using a JEOL (JSM-6360) Zeiss 1530 Gemini instrument equipped with a field emission cathode with a lateral resolution of approximately 3 nm and acceleration voltage 3 kV after sputtering the sample on a silicon wafer (approx. 6 nm). Energy dispersive X-ray (EDX) analysis was performed on a LEO 1530 field emission scanning electron microscope using an X-ray detector. Transmission electron microscopy (TEM) and selected area electron diffraction (SAED) was carried out on a JEOL JEM 2100 (JEOL, Japan) microscope operated at 200 kV. An epoxy resin (EpoFix kit, Struers) was used to prepare specimens for cross-sectional microtomed TEM imaging. Ultrathin sections, 50–70 nm in thickness, of the microstructures were cut with an Ultracut E Reichert-Jung microtome prepared at room temperature using a diamond knife (Drukker) and dropped on a silicon wafer by using a loop. Fourier transform infrared (FTIR) spectra were recorded in the form of pressed KBr pellets in the range of 400–4000 cm^{-1} on a Shimadzu-FTIR Prestige-21 spectrophotometer. The powder X-ray diffraction patterns were obtained using a D8 ADVANCE BROKERaxs X-ray Diffractometer with CuK_α radiation (λ = 1.4506 Å); data were collected at a scan rate of 0.5° min^{-1} in the range of 10–80°. The NMR spectra were recorded in BRUKER AVANCE II 400 FT-NMR spectrometer.

2.2. Synthesis of zinc oxide microstructures

Zinc oxide microstructures have been synthesized in a one pot reaction by hydrolysis of zinc acetate dihydrate as precursor using water and *o*-xylene as the solvent media. An amount of 0.057 g of zinc acetate dihydrate was dissolved in water/*o*-xylene mixture (9 : 1 v/v) in a double-necked round bottom flask by refluxing the mixture in a water bath at 45 °C for 45 min. After dissolving the precursor zinc acetate, potassium hydroxide solution (0.5 g KOH dissolved in 13.5 mL of water) was added to the reaction mixture. The reaction mixture was, then, kept on refluxing for another 15 min; after that, the temperature was increased to 60 °C and the refluxing was continued for another 1 h. Refluxing of the reaction mixture at higher temperature facilitates to achieve smaller size and monodispersity of the constituent ZnO particles in the microstructures. Then, the water bath was removed and the mixture was allowed to stir for 12 h at room temperature. The zinc oxide particles so obtained were retrieved by centrifugation at 10 000 rpm for 5 min and stored in the dark for 3 days before using as catalysts in the corresponding organic reaction.

2.3. Synthesis of the *o*-methylphenyl acetate

Synthesis of *o*-methylphenyl acetate has been carried out by following the procedure described in Vogel's text book.[21] An aliquot of 5 mmol of *o*-cresol was taken in a 50 mL double-necked round bottom flask, dissolved in 25 mL dichloromethane and the reaction mixture stirred for 15 min followed by the addition of 7.5 mmol of triethylamine. Then, acetic anhydride (10 mmol) was added dropwise and the reaction mixture was stirred for 12 h at room temperature. The completion of the reaction was monitored by thin layer chromatographic technique. After completion of the reaction, the post reaction mixture was filtered through a sintered funnel and the residue was washed with ethyl acetate (2 $\times$ 5 mL). The combined ethyl acetate was transferred to a separating funnel, washed with water (3 $\times$ 10 mL) and dried using activated $MgSO_4$. The solvent was removed in a rotary evaporator at room temperature under reduced pressure. The crude product was purified by column chromatography over silica gel (60–120 mesh) using ethyl acetate–petroleum ether as eluent to afford the desired ketone. A schematic presentation of the synthesis of *o*-methylphenyl acetate has been illustrated in Scheme 1.

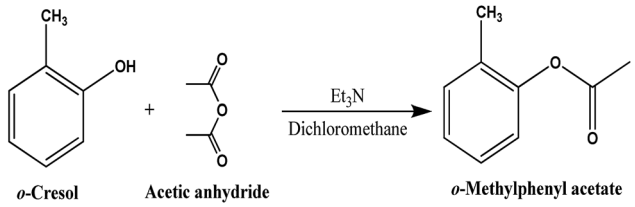

Scheme 1 Schematic presentation of the synthesis of *o*-methylphenyl acetate.

3. Results and discussion

The ZnO microstructures have been synthesised in an one-pot reaction by alkaline hydrolysis of zinc acetate dihydrate employing *o*-xylene-in-water emulsion droplets as the soft templates. Fig. 1 shows the absorption and photoluminescence spectra of the ZnO raspberries in the solid state. The absorption spectrum of the as-prepared particles shows two maxima, one at 254 nm (4.88 eV) and the other at 294 nm (4.22 eV) that arise due to the excitonic transitions between the trapped energy states situated within the confinement region.[22] The optical band edge (band gap 4.4 eV) bears the characteristic electronic transition energy taking place to promote the electrons to the energy states in the conduction band from the valence band, including, excitonic effects. The fluorescence spectrum ($\lambda_{ex} \sim 254$ nm) of ZnO microstructures shows an UV emission band at 372 nm (3.33 eV) that arises due to the radiative recombination of a hole in the valence band and an electron in the conduction band (excitonic emission) and a broad emission in the visible that could be attributed to the presence of multiple surface defects in the microstructures.[23] Therefore, it seems that the formation of microstructures controls the various aspects of the recombination process and favours the radiative transitions from the oxygen vacancies/trap levels in the band gap to give a broad visible luminescence for the assemblies.

The morphology, composition and crystallinity of the as-prepared ZnO assemblies synthesised at the droplet interface are described in Fig. 2. Low resolution scanning electron

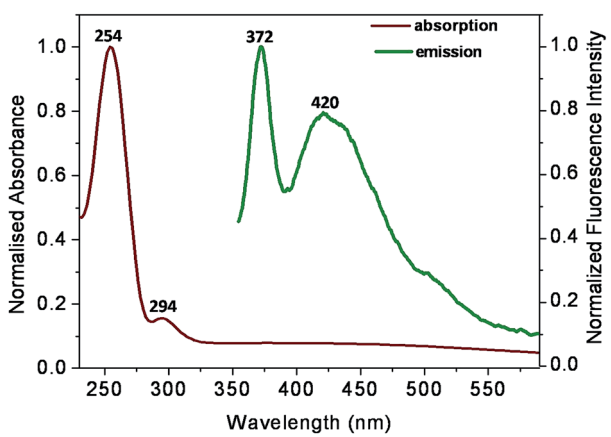

Fig. 1 Absorption and fluorescence spectra of ZnO microstructures in the solid state.

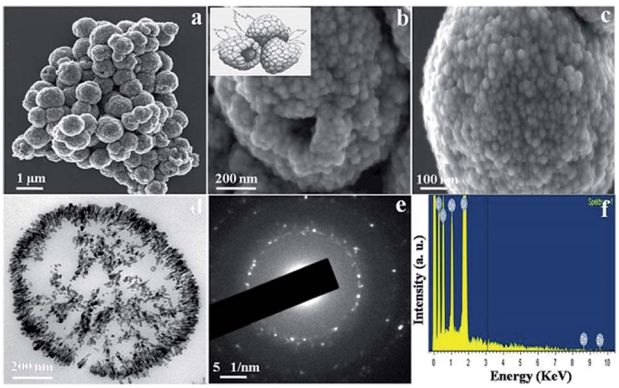

Fig. 2 (a–c) Representative scanning electron microscopic images with increased magnification; (d) microtomed transmission electron micrograph: (e) selected area electron diffraction pattern and (f) energy dispersive X-ray spectrum of the ZnO microstructures.

micrograph (panel a) shows ZnO nanobuilding units are self-assembled into nearly spherical submicrometer-sized aggregates resulting in raspberries-like appearance with average diameter *ca.* 0.7 μm. Careful inspection (panel b) recognises that the assemblies possess well-defined hollow structures and there is, typically, one hole on the surface of each microsphere that appears due to adequate stabilisation of the nanoparticles at interfaces with a high degree of organizational selectivity.[24] Inset shows the photograph of raspberries showing the morphological resemblance with the particles. At higher resolution (panel c), self-assembly of the nanobuilding units on the interface as constructional base and roughened surface of the assemblies are apparent. The microtommed transmission electron micrograph of the cross-section (panel d) of the assemblies exhibit hollow interior of the microstructures bearing spherical cavity, with the thickness of the shell ranging from 40 to 100 nm. The corresponding selected area electron diffraction pattern (panel e) of the as-prepared raspberries reveals the appearance of polycrystalline-like diffraction, which is consistent with reflections (100), (002), (101), (102) and (110), corresponding to the hexagonal wurtzite phase of ZnO particles, indicating that the microstructure is an ordered assembly of small nanocrystal sub-units without crystallographic orientation.[25] The EDX spectrum (panel f) of the hollow microstructures indicates the presence of Zn elements in the composites. The signals of C, O and Si elements come from the as-prepared ZnO, acetate counterions adsorbed onto the particle surface and the silicon wafer employed for the SEM measurement.

The crystallinity and phase of the as-synthesised ZnO microstructures is shown in Fig. 3. The strong reflections shown in the pattern could be indexed to the pure hexagonal phase of Zn with a space group of C_{6v}^4 and cell constants $a = 3.25$ Å, and $c = 5.21$ Å (JCPDS card no. 76-0704), which suggests that the product comprises ZnO nanocrystals with the wurtzite structure.[26]

Fig. 4 shows the FTIR spectrum of the as-prepared ZnO assemblies formed at the interface of emulsion droplets. The presence of a sharp peak at 458 cm^{-1} could be assigned to the stretching vibration of Zn–O bonds in the composites.[27] In

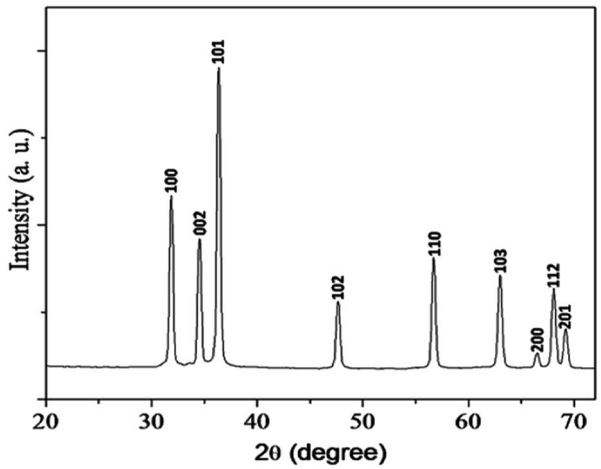

Fig. 3 X-Ray diffractogram of the as-prepared ZnO raspberries.

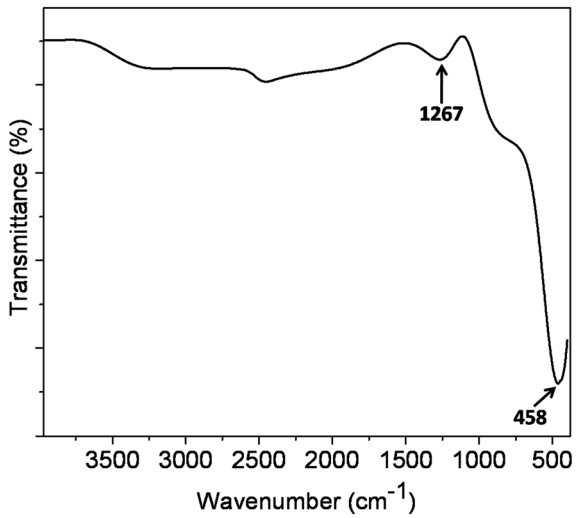

Fig. 4 FTIR spectrum of ZnO raspberries formed at the water/*o*-xylene interface.

addition, a weak absorption at around 1267 cm^{-1} corresponds to C–O stretching frequency of acetate counterions adsorbed onto the metal oxide surface.[28] The absence of any other dominant peak indicates that the particles are merely naked and emphasizes the aptability of the particles for catalytic applications.

A plausible mechanism of the evolution of ZnO microstructures by alkaline hydrolysis of zinc acetate dihydrate in an immiscible liquid pair could be enunciated as follows.

The formation of the assembly was not seen in water (boiling point 100 °C) or *o*-xylene (boiling point 144.4 °C) alone; this indicates oil-in-water emulsion droplets provide the restricted environment at the liquid–liquid interface in harnessing into raspberry-like assemblies.[29] It is now well established in the literature that a liquid–liquid interface is a non-homogeneous region, having a thickness of the order of a few nanometers.[2] The interface between two immiscible liquids, thus, offers an important scaffold for the chemical manipulation and self-assembly of the nanocrystals.[30] During the evolution, the ZnO clusters become, mainly, confined at the vicinity of the interface of the emulsion droplets and subsequently, the evolution of shell-like structure follows. When two ZnO building blocks come together, the capillary forces between them strengthen the agglomerate by van der Waals' forces. The monomers in the inner part of the droplet would diffuse to the surface due to the concentration gradient, resulting in hollow structures, and simultaneously such nanostructures would aggregate and fuse together to form nanometer- or micrometer-sized hollow spheres.[31] The resulting naked hollow spheres with accessibility of both interior and exterior having roughened surface because of their low effective density and high specific surface area possess the potential for promising applications, especially, in catalysis.

The as-prepared ZnO raspberries were employed as Lewis acid catalysts for the Fries rearrangement of aryl ester to *p*-hydroxyaryl ketone. The synthesis of the starting organic compound has been described in the Experimental section. In the catalytic reaction, 40 mg of the catalysts was dispersed with 3.5 mL of 0.1 mM *o*-methylphenyl acetate solution and the mixture was hydrolysed at 55 °C for 5 h under stirring condition. The completion of the reaction was tested by thin the catalytic reaction, 40 mg of the catalysts was dispersed with 3.5 mL of 0.1 mM *o*-methylphenyl acetate solution and the mixture was hydrolysed at 55 °C for 5 h under stirring condition. The completion of the reaction was tested by thin layer chromatographic technique and subsequently, worked up to achieve the desired product. A schematic presentation of the catalytic protocol has been described in Scheme 2.

Fig. 5 shows the ^{1}H and ^{13}C NMR spectra of the rearrangement of the ester in the presence of the catalysts. ^{1}H NMR spectra (panel A) of the ester does not exhibit any characteristic NMR peak around alcoholic region, whereas, a well defined peak at δ 3.481 is seen for the product that confirms the formation of *o*-hydroxy ketone upon rearrangement.[32] Moreover, in the ^{13}C NMR spectra (panel B), the presence of a peak at δ 169 for esteric carbon for the reactant is not seen in the product which further authenticates the rearrangement reaction under the experimental condition. A detailed analysis of the NMR spectra could be enunciated as follows:

3.1. *o*-Methylphenyl acetate

^{1}H (300 Hz, $CDCl_3$; Me_4Si at 25 °C, ppm) $\delta = 2.19$ (s, 3H, H^6), 2.28 (3H, H^4), 3.481 (s, 1H, H^1), 7.01 (1H, H^2), 7.13 (1H, H^5), 7.24 (1H,

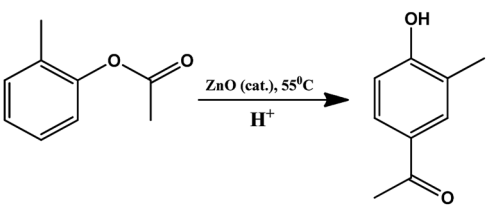

Scheme 2 Catalytic protocol for Fries rearrangement in the presence of ZnO raspberries as catalysts.

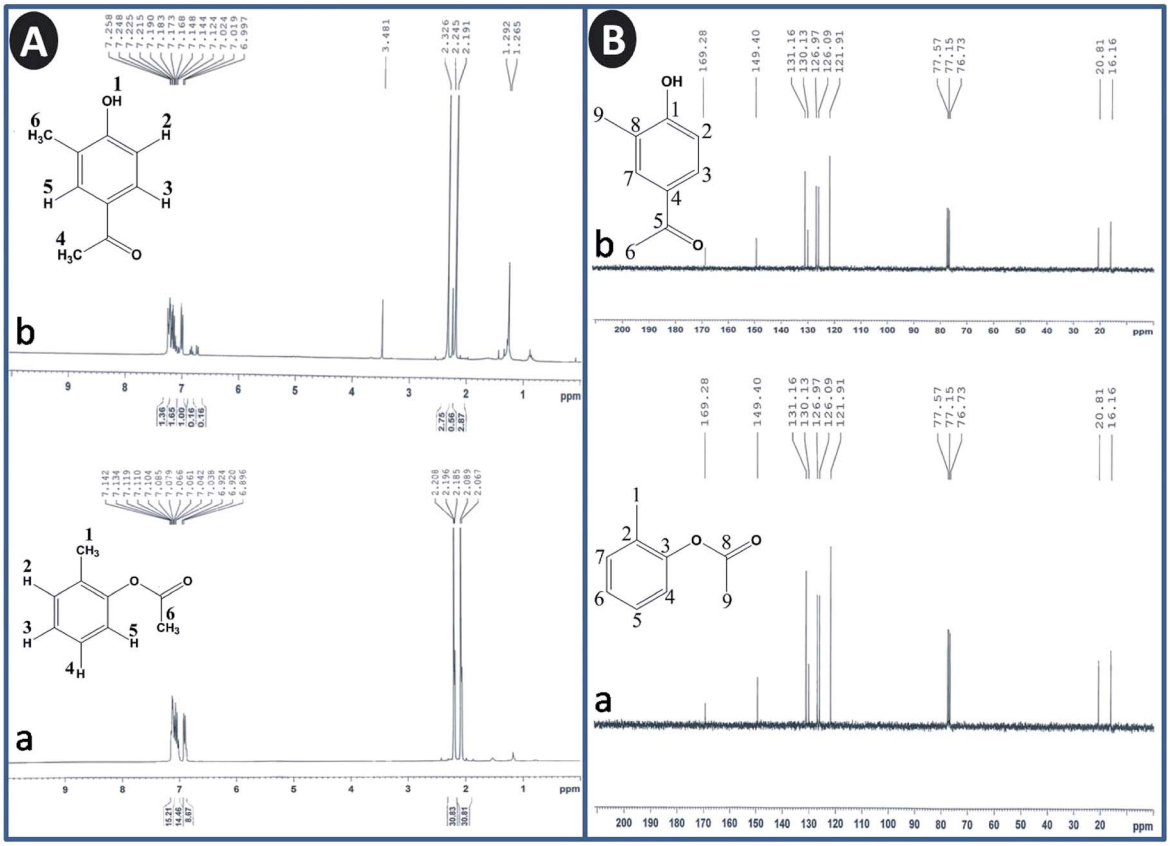

Fig. 5 (A) ^{1}H and (B) ^{13}C NMR spectra of *o*-methylphenyl acetate (a) before and (b) after Fries rearrangement in the presence of ZnO raspberries as catalysts.

H^3); ^{13}C NMR, $\delta = 16.16$ (C^1), 20.81 (C^9), 121.91 (C^4), 126.09 (C^5), 126.97 (C^6), 130.13 (C^2), 131.16 (C^7), 149.49 (C^3), 169.28 (C^8).

3.2. *p*-Hydroxyaryl ketones

^{1}H (300 Hz, $CDCl_3$; Me_4Si at 25 °C, ppm) $\delta = 2.078$ (s, 3H, H^1), 2.196 (s, 3H, H^6), 6.913 (m, 1H, H^2), 7.047 (1H, H^3), 7.127 (1H, H^4), 7.142 (s, 1H, H^5); ^{13}C NMR, $\delta = 16.16$ (C^9), 20.81 (C^6), 121.91 (C^2), 126.09 (C^3), 126.97 (C^8), 130.13 (C^7), 131.16 (C^4), 149.49 (C^1), 169.28 (C^5).

The proposed methodology is capable of providing the desired product in good yields (92–97%). At the end of the reaction, *p*-hydroxyaryl ketones and ZnO microstructures remain in the reaction mixture. In this reaction, submicrometer-sized ZnO assemblies act as heterogeneous catalysts which are inorganic materials. Therefore, the catalysts were separated from the reaction mixture by centrifugation or natural sedimentation at the end of the reaction and subsequent drying in air. It is observed that the assemblies could be reused up to seven cycles of operations without any apparent loss of activity and the catalytic turnover frequency is *ca.* 24.14 per gm of the catalysts. A histogram showing the yield of product for each cycle is presented in Fig. 6. Therefore, it is evident that the as-prepared ZnO raspberries could be projected as catalysts for Fries rearrangement of phenolic esters to *p*-hydroxyphenyl carbonyl compounds with industrially favourable turnover frequency.

It is well-established in the literature that Fries rearrangement is an organic reaction used to convert aryl ester to *o*- and/or *p*-hydroxyaryl-ketones using a Lewis acid catalyst involving the migration of an acyl group of phenolic ester to benzene ring.[33] In the present reaction, ZnO assemblies act as alternative to conventional Lewis acid catalysts. Therefore, the mechanism begins with coordination of the ester to the Lewis acid, followed by a rearrangement which generates an electrophilic acylium

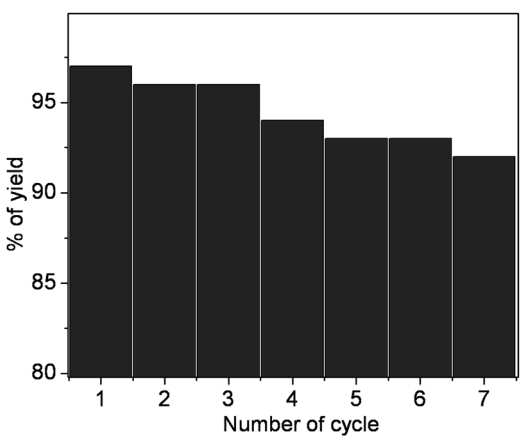

Fig. 6 Histogram showing the yield of product in different cycles of the reusability of the catalysts.

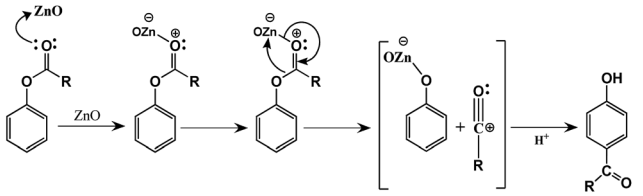

Scheme 3 Schematic representation of the reaction mechanism in the presence of ZnO as catalysts.

cation. The aromatic compound, then, attacks the alkyl cation, selectively, at the *para* position, *via* an electrophilic aromatic substitution. Deprotonation regenerates aromaticity and Brønsted acid work-up regenerate the Lewis acid catalyst provided with the *p*-hydroxyaryl ketonic product.[34] A plausible mechanism of the reaction in the presence of ZnO as catalysts is depicted in Scheme 3.

4. Conclusion

In conclusion, the present methodology based on the formation of *o*-xylene-in-water emulsion droplets could offer a viable platform for the synthesis of submicrometer-sized ZnO assemblies. These hollow and template-free assemblies could be envisaged as greener catalysts in Fries rearrangement for the conversion of phenolic ester to *p*-hydroxyaryl carbonyl compound with high turnover frequency. It is anticipated that the strategy of preparing hollow ZnO assemblies could be utilized as a landscape to the self-assembly of nanobuilding units of other transition metal oxides at the fluid interfaces to explore the application of these light-weight materials in nanotechnology.

Acknowledgements

We gratefully acknowledge financial support from DST, New Delhi (Project no. SR/FT/CS-68/2010).

References

1 E. Katz, A. N. Shipway and I. Willner, in *Nanoscale Materials*, ed. L. M. Liz-Marzan and V. P. Kamat, Kluwer, Norwell, 2003, pp. 317–343.
2 A. Böker, J. He, T. Emrick and T. P. Russell, *Soft Matter*, 2007, **3**, 1231.
3 G. Martino, in *12th International Congress on Catalysis (Studies in Surface Science and Catalysis Series, Vol. 130)*, ed. A. Corma, F. V. Melo, S. Mendioroz and J. L. G. Fierro, Elsevier, Amsterdam, 2000, p. 83.
4 A. J. Gellman and N. Shukla, *Nat. Mater.*, 2009, **8**, 87.
5 G. Schmid, in *Nanoscale Materials in Chemistry*, ed. K. J. Klabunde, Wiley Interscience, New York, 2001, pp. 15–59.
6 H. H. Kung, in *Transition Metal Oxides: Surface Chemistry and Catalysis*, Elsevier, Amsterdam, 2nd edn, 1991.
7 D. Astruc, F. Lu and J. Ruiz Aranzaes, *Angew. Chem., Int. Ed.*, 2005, **44**, 7852.
8 Z. L. Wang, *Appl. Phys. A: Mater. Sci. Process.*, 2007, **88**, 7.
9 K. Fries and G. Finck, *Ber. Dtsch. Chem. Ges.*, 1908, **41**, 4271.
10 S. Paul and M. Gupta, *Synthesis*, 2004, 1789.
11 G. A. Olah, M. Arvanaghi and V. V. Krishnamurthy, *J. Org. Chem.*, 1983, **48**, 3359.
12 V. Rozenberg, T. Danilova, E. Sergeeva, E. Vorontsov, Z. Starikova, K. Lysenko and Y. Belokon, *Eur. J. Org. Chem.*, 2000, 3295.
13 A. Commarieua, W. Hoelderich, J. A. Laffitte and M. P. Dupont, *J. Mol. Catal. A: Chem.*, 2002, **182–183**, 137.
14 M. Kidwai, in *Green Chemistry–Environmentally Benign Approaches*, InTech, Europe, Croatia, 2012, ch. 6.
15 S. Kobayashi, M. Moriwaki and I. Hachiya, *Chem. Commun.*, 1995, 1527.
16 J. H. Clark, M. G. Dekamin and F. M. Moghaddam, *Green Chem.*, 2002, **4**, 366.
17 H. W. Kouwenhoven, R. Prins and A. Vogt, *Appl. Catal., A*, 1995, **123**, 37.
18 J. Kato, H. Kakehata, Y. Maekawa and T. Yamashita, *Chem. Commun.*, 2006, 4498.
19 B. M. Khadilkar and V. R. Madyar, *Synth. Commun.*, 1999, **7**, 1195.
20 R. H. Jitendra, J. N. Susheel and M. S. Manikrao, *Tetrahedron Lett.*, 2001, **42**, 1979.
21 A. I. Vogel, in *Textbook of Practical Organic Chemistry*, ed. B. S. Furniss, A. Hannaford, P. W. G. Smith and A. R. Tatchel, 5th edn, 1996.
22 A. P. Alivisatos, *Science*, 1996, **271**, 933.
23 M. L. Kahn, T. Cardinal, B. Bousquet, M. Monge, V. Jubera and B. Chaudret, *ChemPhysChem*, 2006, **7**, 2392.
24 W. H. Binder, *Angew. Chem., Int. Ed.*, 2005, **44**, 5172.
25 M. Y. Ge, H. P. Wu, L. Niu, J. F. Liu, S. Y. Chen, P. Y. Shen, Y. W. Zeng, Y. W. Wang, G. Q. Zhang and J. Z. Jiang, *J. Cryst. Growth*, 2007, **305**, 162.
26 M. Goano, F. Bertazzi, M. Penna and E. Bellotti, *J. Appl. Phys.*, 2007, **102**, 083709.
27 M. Andres Verges, A. Mifsud and C. J. Serena, *J. Chem. Soc., Faraday Trans.*, 1990, **86**, 959.
28 F. Zaera, *Chem. Phys. Lett.*, 1985, **121**, 464.
29 A. K. Boal, F. Ilham, J. E. De Rouchey, T. Thurn-Albrecht, T. P. Russel and V. M. Rotello, *Nature*, 2004, **404**, 746.
30 D. Nykypanchuk, M. M. Maye, D. van der Lelie and O. Gang, *Nature*, 2008, **451**, 549.
31 H. Jie, S. Genping and G. Rong, *Adv. Mater.*, 2006, **18**, 3140–3144.
32 W. Kemp, in *NMR in Chemistry: A Multinuclear Introduction*, New York, 1988, pp. 141–145.
33 J. March, in *Advanced Organic Chemistry*, John Wiley & Sons, Chichester, 3rd edn, 1985, S. 499ff.
34 M. Guisne and G. Perot, in *The Fries Rearrangement*, ed. R. A. Sheldon and H. Bekkum, New York, 2001, pp. 211–215.

RSC Advances

COMMUNICATION

Cite this: *RSC Adv.*, 2014, **4**, 61404

Fluid interface-mediated nanoparticle membrane as an electrochemical sensor†

Mohammed Ali, Koushik Barman, Sk. Jasimuddin and Sujit Kumar Ghosh*

Received 10th October 2014
Accepted 7th November 2014

DOI: 10.1039/c4ra12149j

www.rsc.org/advances

A poly(ethyleneglycol) (PEG-13)-stabilised magnetic Fe_3O_4 nanoparticle decorated ultra-thin membrane has been devised at the water/chloroform interface by ligand cross-linking between pendant hydroxyl groups of PEG with terephthaloyl chloride. This robust nanoparticle-decorated membrane has been employed as an electrochemical sensor for the detection of L-Dopa up to nanomolar concentration.

1. Introduction

The fabrication of membranes *via* self-assembly of nanoscale materials is of interest for delivery vessels, size-selective separation and purification, controlled-release materials, sensors and catalysts, scaffolds for tissue engineering, low dielectric constant materials for microelectronic devices, antireflective coatings and proton exchange membranes for polymer electrolyte membrane fuel cells *etc.*[1–4] Recently, nanocrystalline iron oxides, composites and related materials have received special attention due to their viability as a platform for electrochemical, magnetic, and chemical biosensors.[5,6] While many kinds of nanoparticles, such as, metal, metal oxide and semiconductor nanoparticles have been used for constructing electrochemical sensors and biosensors, these nanoparticles play different roles in different sensing systems.[7] Since, the electrochemical detection is based on the current changes by modifying the electrode surface covered with a thin layer of particles due to the presence of chemical components of the reacting system, therefore, it has to make sure that, all the particles should be well-connected to each other so that the impulse could be transmitted throughout. Based on these conceptives, a robust and ultrathin membrane made up of nanoparticles could be an effective choice for electrochemical sensing applications rather than, simply, attaching a layer of particles on the electrode surface. Such membrane-based electrochemical sensor is not only effective but also more sensitive than the conventional particle-based sensors,[8] while the fabrication of such membrane and draping it onto the electrode surface remain challenging.

L-Dopa is the immediate precursor of the neurotransmitter dopamine, that plays a very crucial role in the functioning of the central nervous, cardiovascular, renal, and hormonal systems, as well as in drug addiction and Parkinson's disease.[9] Thus, it becomes imperative for neuro and analytical scientists to find out a means to detect the presence of L-Dopa in human body up to trace amount.[10] Several techniques for the detection of L-Dopa have been described in the literature, including, flow injection method,[11] fluorescence spectroscopy,[12] cyclic voltammetry[13,14] and so on. While different types of membranes *e.g.*, Nafion membranes,[15] enzyme collagen membranes,[16] bilayer lipid membranes,[17] gallium arsenide electrodes functionalised with supported membranes[18] have, conventionally, been used for electrochemical sensing and nanoparticle-decorated ultrathin membrane have been employed to study their permeability and elasticity,[19] nanofiltration,[20] triggered release from liposomes,[21] targeted transfection[22] and so on; we have been interested to exploit nanoparticle-membrane as electrochemical sensor. In this communication, we have reported the fabrication of Fe_3O_4 nanoparticle-decorated ultrathin membrane at the water/chloroform interface by terephthaloyl chloride and the membrane has been employed for electrochemical detection of L-Dopa up to nanomolar concentration.

2. Experimental

Reagents and instruments

All the reagents used were of analytical reagent grade. L-Dopa and phosphoric acid (Sigma Aldrich), PEG-13 (Broad Pharm, USA), anhydrous $FeCl_3$ and ammonium ferrous sulphate (Merck, India) were used without further purification.

Department of Chemistry, Assam University, Silchar-788011, India. E-mail: sujit.kumar.ghosh@aus.ac.in

† Electronic supplementary information (ESI) available: Instrumentation and experimental details, cyclic voltammetry and differential pulse voltammetry. See DOI: 10.1039/c4ra12149j

Chloroform and ammonia (S. D Fine Chemicals, India) and sodium perchlorate (Sisco Research Laboratories, India) were used as received. An aliquot of 0.1 M phosphate buffer saline (PBS) was prepared by mixing of equimolar solution of phosphoric acid and sodium perchlorate followed by dropwise addition of sodium hydroxide. Double distilled water was used throughout the course of the experiment. The temperature was 298 ± 1 K for all experiments.

The membrane was observed by optical microscope (Olympus BX 61) equipped with a high resolution DP70 digital charge coupled device (CCD) camera and images were processed using Aldus Photostyler 3.0 software. Scanning electron micrographs were recorded by using JEOL JSM-6360 instrument equipped with a field emission cathode with a lateral resolution of approximately 3 nm and acceleration voltage 3 kV after sputtering the sample on silicon wafer with carbon (approx. 6 nm). Thin films were prepared by drop-coating the membrane from water/chloroform interface and transferred onto silicon wafer with the help of a micropipette. Transmission electron microscopy was carried out on a JEOL JEM-2100 microscope with a magnification of 200 kV. Samples were prepared by placing a drop of solution on a carbon coated copper grid and dried overnight under vacuum. High-resolution transmission electron micrographs and selected area electron diffraction pattern were obtained using the same microscope. Fourier transform infrared (FTIR) spectra were recorded in the form of pressed KBr pallets in the range (400–4000 cm^{-1}) in Shimadzu-FTIR Prestige-21 spectrophotometer. Electrochemical measurements were performed by a CHI-660C electrochemical workstation. An Ag/AgCl electrode (in 3.0 M KCl) and a Pt wire were used as reference and auxiliary electrodes, respectively. Catalytic reactions were performed by the immobilized nanoparticles or nanocomposites over a 4-aminothiophenol monolayer modified gold working electrode where 0.1 M phosphate buffer saline (pH ~ 7.5) was used as electrolyte and the scan rate was 100 mV s^{-1}.

Synthesis of Fe_3O_4 nanoparticles

Polyethylene glycol (PEG-13)-stabilised iron oxide nanoparticles were synthesised by modification of the procedure reported by Gillich *et al.*[23] In a typical synthesis, 1.99 g (0.01 mol) $(NH_4)_2$-$Fe(SO_4)_2 \cdot 6H_2O$ and 5.41 g (0.02 mol) $FeCl_3 \cdot 6H_2O$ were dissolved in 50 mL distilled water in a beaker so that the molar ratio of $Fe^{2+} : Fe^{2+} = 1 : 2$. In a separate beaker, an aqueous NH_4OH (30% v/v) solution (1.5 M) was prepared. Then, polyethylene glycol (0.1 M) was added at a ratio of 1 : 10 to both the above solutions to get precursor solutions I and II respectively. After that, precursor solution II was added to solution I dropwise under stirring condition at 40 °C; just after mixing the solutions, colour of the solution changes from light brown to black indicating the formation of Fe_3O_4 nanoparticles. The stirring was continued for another 45 min and the solution was cooled to room temperature. The precipitate so-obtained was washed thrice by centrifugation and redispersed in distilled water. The particles are spherical or nearly spherical and the size of the particles was found to be 5 ± 0.5 nm.

Synthesis of membrane

Ultrathin membrane made up of PEG-coated Fe_3O_4 nanoparticles were synthesised at water/chloroform interface by intermolecular polymerization between pendant –OH groups of PEG anchored onto Fe_3O_4 nanoparticles surfaces with the help of terephthaloyl chloride (TC), a well-known ligand cross-linker. In a typical method, 2 mL of Fe_3O_4 hydrosol (0.25 mM) was taken in a test tube and equal volume of chloroform containing small amount of terephthaloyl chloride was mixed and shaken vigorously. After about 2 min, the mixture was allowed to settle and after few moments, the formation of a membrane has been observed at the interface.

3. Results and discussion

The structure and morphology of the membrane has been characterised by optical microscopy, scanning electron microscopy (SEM), transmission electron microscopy (TEM) and high resolution transmission electron microscopic images (HRTEM) as shown in Fig. 1. Panel a shows the optical microscope image of the as-prepared membrane. The membrane so-formed at the interface was collected by micropipette and kept suspended in chloroform in the cavity of a glass slide. An ultrathin membrane can, clearly, be observed; the ridges on the membrane arises during the transfer of the membrane by micropipette on the glass slide, which, in turn, support robustness of the membrane.[19] Typical SEM image of the membrane (panel b) exhibit the formation of an intact and robust membrane at water/chloroform interface.[22] Panel c is the representative transmission electron micrograph of the membrane which shows compact and regular monolayer arrangement of the nanoparticles in the membrane.[24] The

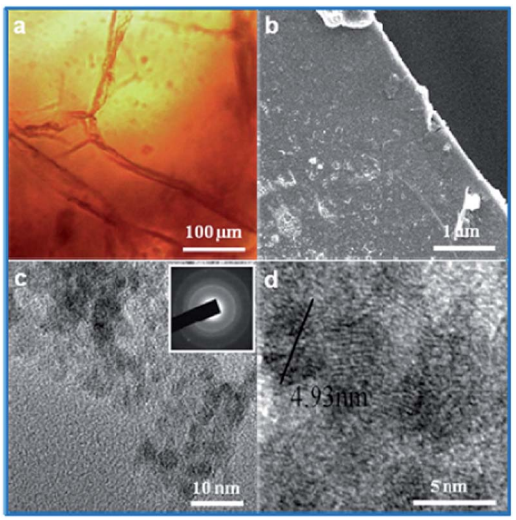

Fig. 1 (a) Optical micrograph, (b) scanning electron micrograph, (c) transmission electron micrograph and (d) high resolution transmission electron micrograph of the Fe_3O_4 nanoparticle-decorated membrane. Inset in panel c shows the selected area electron diffraction pattern of the membrane.

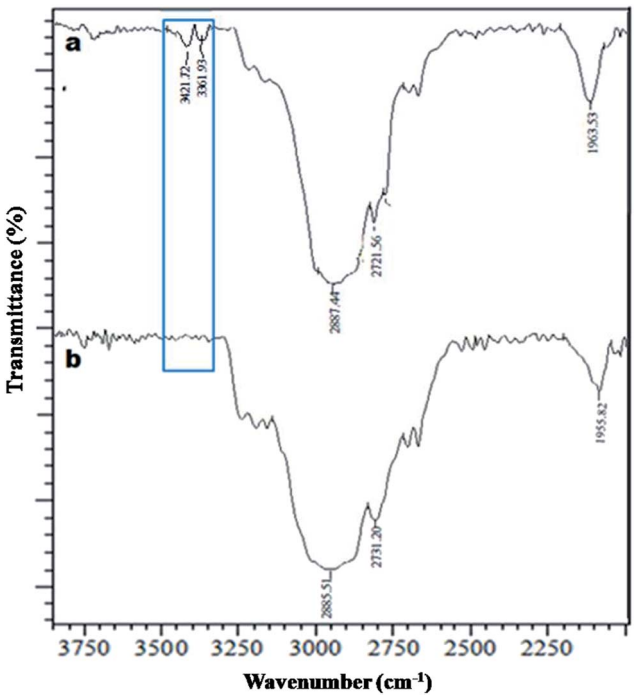

Fig. 2 FTIR spectra of PEG-stabilised Fe_3O_4 nanoparticles (a) before and (b) after cross-linking.

selected area electron diffraction (SAED) pattern shown in the inset exhibits five distinct diffraction rings of (220), (311), (420), (511) and (440) confirmed a typical magnetite crystalline structure.[25] Panel d is the high resolution TEM image of the membrane which, further, confirms two dimensional ordering of the Fe_3O_4 nanoparticles in the membrane.[26]

The ligand cross-linking between the chain-end hydroxyl groups of PEG *via* terephthaloyl chloride has been monitored by FTIR spectroscopy. Fig. 2 shows the overlaid FTIR spectra of PEG-13 stabilised Fe_3O_4 nanoparticles (trace a) and nanoparticle-decorated membrane formed after cross-linking (trace b). It is observed that, the peaks at *ca.* 3360 and 3420 cm^{-1} corresponding to –O–H stretching is disappeared indicating successful cross-linking between hydroxyl groups of PEG with the acyl chloride moiety of the terephthaloyl chloride molecules.[27]

It is well-established in the literature that ultrasmall particles strongly segregate to the interface of immiscible fluids, driven by a reduction of interfacial energy.[1–3] When such interfacial assembly of nanoparticles takes place in a 2D interface (a flat surface), thin films of nanoparticles could be produced *in situ* at interfaces between immiscible fluids. Such membranous structure may be less stable, but when the nanoparticles used in these interfacial assemblies are decorated with functional ligands, the assemblies can be stabilized and transformed into robust materials by performing chemistry on the functional groups contained within the ligand structure.[1,3] In this experiment, the PEG-13 stabilised Fe_3O_4 nanoparticle-decorated membrane at the water/chloroform interface has been stabilized by cross-linking the chain-end hydroxyl groups of PEG with two acyl chloride moieties of terephthaloyl chloride, as represented in Scheme 1.

The magnetism of the membrane acquired, by virtue, of its magnetic nanoparticles as building blocks, was investigated by applying an external magnetic field (Fig. 3). A homogenous uniform membrane with over a large area (~55.4 cm^2) is seen in the absence of the magnet (panel a). However, the membrane becomes folded towards a bar magnet when it is placed nearby and unfolded when the magnet bar is taken away. The membrane folding and unfolding is observed even up to ten cycles of operations pointing out the mechanical robustness of the membrane through magnetic actuation of super paramagnetic iron oxide nanoparticle membrane constituted of cross-linked ultrasmall particles. Amstad *et al.*[21] have demonstrated triggered release from reversibility of oxide nanoparticle containing membranes. Therefore, magneto-responsibility of the liposomes could be exploited in the near future for the development of efficient drug carriers that can deliver anticancer agents specifically into cancerous tissues exposed to a magnetic field.[1,4]

Now, the nanoparticle-decorated ultrathin membrane was employed as an electrochemical sensor for the determination of L-Dopa upto nanomolar concentration (Fig. 4). The modification of the gold electrode with the membrane and its electrochemical characterisation are described in ESI 1.† A study of electrocatalytic oxidation of L-Dopa at different pH (ESI 2†) indicates that the interaction between membrane-modified gold electrode and L-Dopa is optimum at pH 7.0. Panel a

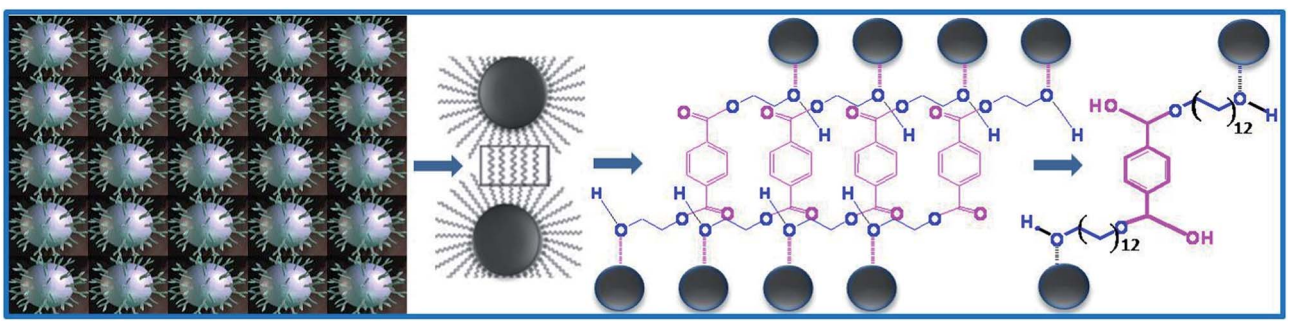

Scheme 1 Schematic presentation of formation of nanoparticle-decorated membrane by cross-linking of chain end hydroxyl groups of PEG with acyl chloride moiety of terephthaloyl chloride *via* ester linkage formation.

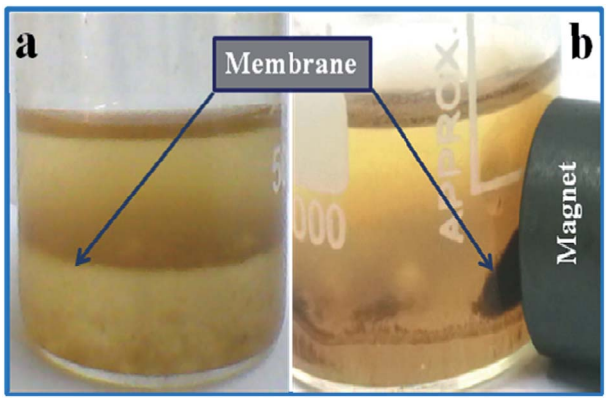

Fig. 3 Response of the nanoparticle-decorated ultrathin membrane in the (a) absence and (b) presence of a bar magnet.

shows the cyclic voltammogram of 1.0 mM L-Dopa in 0.1 M PBS (pH ~ 7.0) on bare (black curve) and membrane-modified gold electrode (red curve). The appearance of a pair of weak redox peak was observed with a peak-to-peak separation, $\Delta E_p = 230$ mV on the bare gold electrode. However, a well-defined irreversible redox wave ($\Delta E_p = 188$ mV) was seen on the modified electrode. It is noted that the anodic peak potential shifts negatively (26 mV) and the anodic peak current is higher (15 μA) in comparison with the bare electrode, which suggests that the membrane-modified gold electrode shows electrocatalytic oxidation of L-Dopa (L-Dopa + $2H_2O$ → Dopaquinone + $4H^+$ + $4e^-$). The transfer of four electrons for L-Dopa oxidation was confirmed by comparing the current height with the $[Fe(CN)_6]^{3-/4-}$ redox couple under similar measurement conditions.[28] The scan rate dependence of oxidation current of L-Dopa is proportional to the square root of the scan rate indicating that the oxidation is diffusion-controlled.[29] Panel b shows the cyclic voltammetric responses of the membrane-modified electrode for L-Dopa at different scan rate. Inset shows a plot of oxidation current with increase in concentration of L-Dopa. It is seen that, the oxidation current of L-Dopa increases, linearly, with increase in concentration in the range of 1–4.5 μM. The concentration of L-Dopa could be determined in the range 0.05–10 μM and the limit of detection (LOD, an average of three determinations) was obtained as 9.5 nM using equation $3\sigma/m$, where, σ is the standard deviation of the measurement and m is the slope of the calibration curve, I_p (μA) = $0.122C$ (μM) + 6.608 and $R^2 = 0.996$. A comparative account of the sensing capabilities for the determination of L-Dopa in the presence of different materials and methods is presented in ESI 3.† Moreover, it is seen that nanoparticle-decorated membrane is able to determine L-Dopa and ascorbic acid in binary mixtures of the compounds, linearly, in an appreciable concentration range (ESI 4†). Therefore, it could be inferred that, the nanoparticle-decorated membrane could, even, be exploited as an electrochemical sensor for simultaneous determination of L-Dopa and ascorbic acid in a binary mixture of the compounds.

4. Conclusion

In summary, water/chloroform interface has been exploited as a viable platform for the fabrication of Fe_3O_4 nanoparticle-decorated robust, ultrathin membrane by cross-linking the chain-end hydroxyl groups of PEG ligands attached onto nanoparticle surface with the help of terephthaloyl chloride as the ligand cross-linker. This nanoparticle-decorated ultrathin membrane has been, successfully, employed for electrochemical detection of L-Dopa (and also L-Dopa and ascorbic acid simultaneously) up to nanomolar level concentrations. The membrane could be manipulated in the near future using external magnetic field, providing a convenient and gentle means to utilise as efficient delivery vehicles for various therapeutic agents, particularly, in cancer therapy.

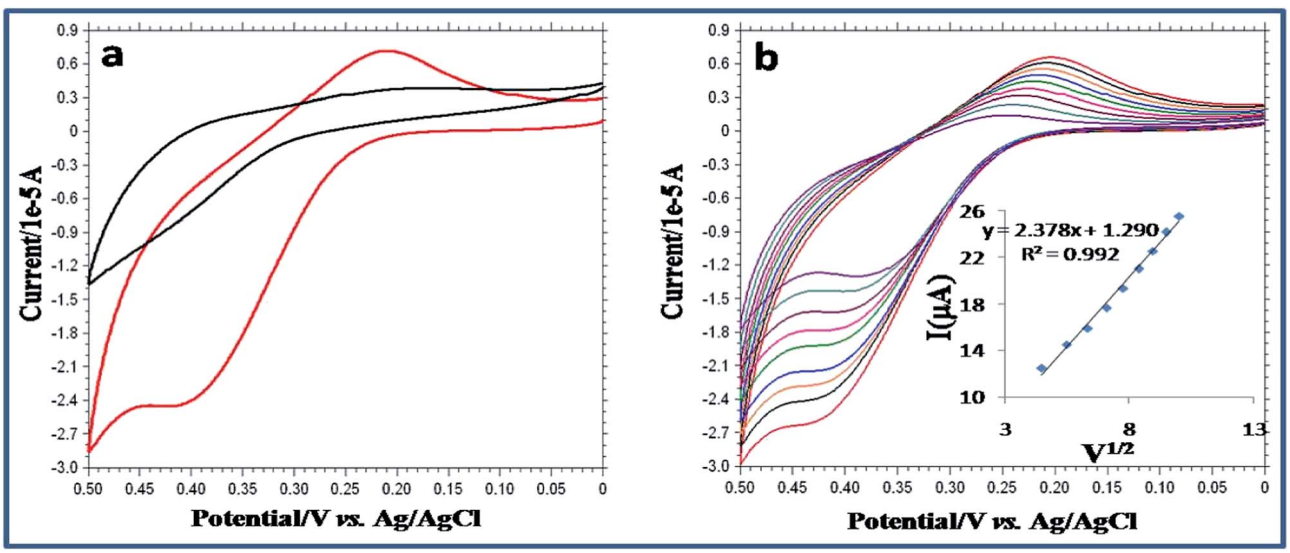

Fig. 4 (a) Cyclic voltammogram of 1.0 mM L-Dopa (at pH ~ 7.0) at bare (black curve), and membrane-modified gold electrode (red curve); and (b) cyclic voltammetry of L-Dopa at different scan rate at membrane-modified gold electrode.

Acknowledgements

We gratefully acknowledge financial support from DST, New Delhi (Project no. SR/FT/CS-68/2010).

Notes and references

1 D. Wang and H. Möhwald, *J. Mater. Chem.*, 2004, **14**, 459–468.
2 W. H. Binder, *Angew. Chem., Int. Ed.*, 2005, **44**, 5172–5175.
3 A. Böker, J. He, T. Emrick and T. P. Russell, *Soft Matter*, 2007, **3**, 1231–1248.
4 P. van Rijn, M. Tutus, C. Kathrein, L. Zhu, M. Wessling, U. Schwaneberg and A. Böker, *Chem. Soc. Rev.*, 2013, **42**, 6578–6592.
5 S. Laurent, D. Forge, M. Port, A. Roch, C. Robic, L. Vander Elst and R. N. Muller, *Chem. Rev.*, 2008, **108**, 2064–2110.
6 V. Urbanova, M. Magro, A. Gedanken, D. Baratella, F. Vianello and R. Zboril, *Chem. Mater.*, 2014, DOI: 10.1021/cm500364x.
7 M. Pumera, in *Nanomaterials in electrochemical sensing and biosensing*, CRC Press, Boca Raton, USA, 2013.
8 X. Luo, A. Morrin, A. J. Killard and M. R. Smyth, *Electroanalysis*, 2006, **18**, 319–326.
9 P. Damier, E. C. Hirsch, Y. Agid and A. M. Graybiel, *Brain*, 1999, **122**, 1437–1448.
10 B. J. Venton and R. M. Wightman, *Anal. Chem.*, 2003, **224**, 414A–421A.
11 M. F. S. Teixeira, L. H. Marcolino-Júnior, O. Fatibello-Filho, E. R. Dockal Márcio and F. Bergamini, *Sens. Actuators, B*, 2007, **122**, 549–555.
12 A. Coskun and E. U. Akkaya, *Org. Lett.*, 2004, **6**, 3107–3109.
13 F. R. Leite, C. M. Maroneze, A. B. de Oliveira, W. T. dos Santos, F. S. Damos and C. Silva Luz Rde, *Bioelectrochemistry*, 2012, **86**, 22–29.
14 X. Yan, D. Pan, H. Wang, X. Bo and L. Guo, *J. Electroanal. Chem.*, 2011, **663**, 36–42.
15 R. C. Mercado and F. Moussy, *Biosens. Bioelectron.*, 1998, **13**, 133–145.
16 D. R. Thevenot, R. Sternberg, P. R. Coulet, J. Laurent and D. C. Gautheron, *Anal. Chem.*, 1979, **51**, 96–100.
17 D. P. Nikolelis and U. J. Krull, *Electroanalysis*, 1993, **5**, 539–545.
18 D. Gassull, A. Ulman, M. Grunze and M. Tanaka, *J. Phys. Chem. B*, 2008, **112**, 5736–5741.
19 Y. Lin, H. Skaff, A. Böker, A. D. Dinsmore, T. Emrick and T. P. Russell, *J. Am. Chem. Soc.*, 2003, **125**, 12690–12691.
20 J. He, X. M. Lin, H. Chan, L. Vukovic, P. Kräl and H. M. Jaeger, *Nano Lett.*, 2011, **11**, 2430–2435.
21 E. Amstad, J. Kohlbrecher, E. Müller, T. Schweizer, M. Textor and E. Reimhult, *Nano Lett.*, 2011, **11**, 1664–1670.
22 M. Delcea, N. Sternberg, A. M. Yashchenok, R. Georgieeva, H. Bäumler, H. Möhwald and A. G. Skirtach, *ACS Nano*, 2012, **6**, 4169–4180.
23 T. Gillich, C. Acikgöz, L. Isa, A. D. Schlüter, N. D. Spencer and M. Textor, *ACS Nano*, 2013, **7**, 316–329.
24 M. Ali, S. Bora and S. K. Ghosh, *Langmuir*, 2014, **30**, 10449–10455.
25 R. M. Cornell and U. Schwertmann, *The Iron Oxides*, VCH, Weinheim, 2nd edn, 2003.
26 B. Samanta, D. Patra, C. Subramani, Y. Ofir, G. Yesibug, A. Sanyal and V. M. Rotello, *Small*, 2009, **5**, 685–688.
27 S. T. Hussain, M. Iqbal and M. Mazhar, *J. Nanopart. Res.*, 2009, **11**, 1383–1391.
28 J. P. E. Spencer, P. Jenner, S. E. Daniel, A. J. Lees, D. C. Marsden and B. Halliwell, *J. Neurochem.*, 1998, **71**, 2112–2122.
29 M. Mazloum-Ardakani, M. Yavari, M. Ali Sheikh-Mohseni and B. F. Mirjalili, *Catal. Sci. Technol.*, 2013, **3**, 2634–2638.

Langmuir

Article

pubs.acs.org/Langmuir

Composite-Walled Magnetic Microcapsules at the Water−Toluene Interface by Ligand Polymerization

Mohammed Ali, Sangita Bora, and Sujit Kumar Ghosh*

Department of Chemistry, Assam University, Silchar-788011, India

ABSTRACT: The liquid−liquid interface has been exploited as a platform for devising gold and iron oxide nanoparticle (NP)-decorated composite microcapsules (MCs) by cross-linking between −OH groups of poly(ethylene glycol) (PEG) attached to the iron oxide (Fe_3O_4) nanoparticle surface and starch attached to the gold (Au) nanoparticle surface in the presence of terephthaloyl chloride as a cross-linker. These nanoparticle-decorated capsules form a shell of both types of nanoparticles with water as the minor phase and toluene as the major phase. The morphology of these capsules has been characterized by optical, transmission, and scanning electron microscopy images, and the polymerization reaction has been established by UV−vis and FTIR spectroscopic studies. The magnetic behavior of the capsules has been illustrated by using an external magnetic field to tailor the magnetic control of the capsules. The encapsulated phase was impregnated with dye molecules of three different sizes, viz., fluorescein isothiocyanate and its dextran conjugates, to investigate the permeability of the capsule wall by fluorescence spectroscopy. Interestingly, the microcapsules exhibit size-selective permeability across the capsule wall that points to their plausible applications in controlled encapsulation and release.

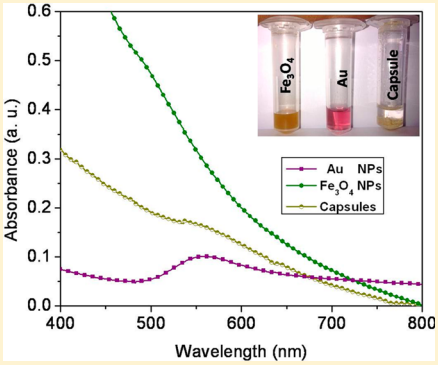

1. INTRODUCTION

The self-assembly of colloidal particles at fluid interfaces offers a straightforward pathway for fabricating novel materials that have attracted immense interest in academic, scientific, and industrial fields due to their advanced technological applications, e.g., targeted delivery vehicles, tracking, diagnostics, microreactors, filters, biomedical engineering, catalysis, and so forth.[1−3] About a century ago, Pickering discovered that colloidal solid particles could be adsorbed onto the liquid−liquid interface to stabilize emulsion droplets to minimize the Helmholtz free energy.[4,5] As a result, colloidal particles localize at the interface, forming a shell made up of colloidal building blocks (both organic and inorganic) leading to the fabrication of microcapsules which makes it possible to achieve significant control over the physical properties of nanodimensional shells.[6−8] The effectiveness in stabilizing the droplets depends on parameters such as the particle size, interparticle interactions, and particle wettability by both the aqueous and oil phases.[9] Due to the advancement of nanoscale synthesis strategies,[10] nanoparticles with diverse morphologies and chemical composition could be exploited for the fabrication of microcapsules with distinct functionalities. These hollow microcapsules provide a means of encapsulation and open up the possibility of harnessing controlled nanoparticle release in a range of novel applications.[11]

Several approaches have been found in the literature to fabricate stable capsules using magnetic iron oxide NPs based on the interfacial assembly of nanometer-sized objects in three dimensions. Duan and coworkers[12] fabricated magnetic-nanoparticle-decorated capsules at the interfaces of water-in-toluene droplets by gelating the water phase with agarose, and the permeability of the capsules can be tailored through the variation of the dimension of the colloidal particles. Koo and colleagues[13] reported the preparation of magnetic microcapsules, based on double emulsions comprising a chloroform core and an iron oxide (γ-Fe_2O_3) nanoparticle-embedded polymer shell, which are reversibly swellable upon repetitive drying and hydration. Samanta and colleagues[14] reported the fabrication of magnetic colloidosomes by cross-linking alkyne- and azide-functionalized Fe_3O_4 nanoparticles at a water−oil interface using click chemistry under ambient conditions. Shi et al.[15] have reported the combination of a layer-by-layer self-assembly method utilizing dendrimer chemistry to fabricate targeted shell-cross-linked iron oxide NPs for in vivo magnetic resonance imaging of tumors. Zhou et al.[16] have synthesized superparamagnetic Fe_3O_4 nanoparticles prepared by a classical coprecipitation method to prepare magnetic Pickering emulsions and investigated the effects of the particle concentration, oil/water volume ratio, and oil polarity on the type, stability, composition, and morphology of these functional emulsions. Hu et al.[17] synthesized iron oxide-containing double-emulsion capsules that can release hydrophilic doxorubicin and hydrophobic paclitaxel remotely triggered by a high-frequency magnetic field and energy via internalized iron oxide nanoparticles for magneto-chemotherapy/hyperthermia with multiple drugs. Kong and colleagues[18] have described hollow capsules containing the desired anticancer drugs together with magnetic nanoparticles, which can provide a powerful magnetic

Received: May 11, 2014
Revised: July 27, 2014
Published: August 19, 2014

   dx.doi.org/10.1021/la5018054 | *Langmuir* 2014, 30, 10449−10455

vector for penetration into a tumor and on-demand drug release upon external radio frequency stimulus. Gorin and colleagues[19] have reported nanocomposite microcapsule shells composed of iron oxide together with gold nanoparticles and established the effect of a magnetic field on the microcapsule concentration along with the sensitivity of the capsules to laser irradiation. On the basis of these perspectives, it is interesting to employ gold and iron oxide nanoparticles as the constituent particles for the formation of microcapsules because the interfacial communication between the nanoscale Au and Fe_3O_4 results in a multimodal platform with magnetic–plasmonic bifunctionality.[20,21] Moreover, the magnetism of Fe_3O_4 NPs is enhanced via interfacial interaction with Au NPs, making the capsules more magnetic in nature.[22] The unique properties of both the iron oxide and gold result in a versatile platform for use as MRI contrast agents and a nanoheater.[23] Therefore, the capsule wall consisting of both Au and Fe_3O_4 contains both magnetically and optically active NPs, which show high potential applications to drug delivery and biomedical imaging.[24−26]

In this article, we have reported the fabrication of composite microcapsules consisting of plasmonic gold and magnetic iron oxide nanoparticles at a water–toluene interface by ligand polymerization. The formation of the capsules has been characterized by UV–vis specroscopy, Fourier transform infrared (FTIR) spectroscopy, optical microscopy, transmission electron microscopy (TEM), and scanning electron microscopy (SEM) images. The response of the MCs in the presence of a bar magnet indicates that the capsules can be manipulated using an external magnetic field. To study the efficacy of these assemblies, the permeability of the capsule wall has been unraveled using dye molecules of three different sizes, and the size-selective permeability of the capsule wall has been demonstrated.

2. EXPERIMENTAL SECTION

2.1. Reagents and Instruments. All of the reagents used were of analytical grade. Ferric chloride ($FeCl_3·6H_2O$), ammonium ferrous sulfate ($(NH_4)_2Fe(SO_4)_2·6H_2O$), starch, chloauric acid ($HAuCl_4·3H_2O$), sodium borohydride ($NaBH_4$), terephthaloyl chloride, and fluorescein isothiocyanate (FITC) and its dextran conjugates (FITC-D 40S and FITC-D 2000S) were purchased from Sigma-Aldrich and used as received. Polymer PEG-13 was obtained from BroadPharm (San Diego, CA) and used without any further purification. Ammonium hydroxide and toluene were purchased from S. D. Fine Chemicals, India.

The UV–vis spectra for all samples were recorded in the solid state on a Shimadzu UV-1601 digital spectrophotometer (Shimadzu, Japan). Fluorescence spectra were recorded ($\lambda_{ex} \approx 490$ nm, slit width 5/5 nm) with a PerkinElmer LS-45 spectrofluorometer (PerkinElmer, USA). Transmission electron microscopy (TEM) was performed on carbon-coated copper grids with a Zeiss CEM 902 operated at 80 kV. Samples were prepared by placing a drop of solution on a carbon-coated copper grid. Fourier transform infrared (FTIR) spectra were recorded in the form of pressed KBr pellets in the range of 400–4000 cm^{-1} with a Shimadzu-FTIR Prestige-21 spectrophotometer. The capsules were observed with an Olympus BX 61 optical microscope (Olympus, Japan) equipped with a high-resolution DP 70 digital charge-coupled device (CCD) camera, and the images were processed using Aldus Photostyler 3.0 software. Scanning electron micrographs were taken with a JEOL JSM-6360 (JEOL, Japan) at an accelerating voltage of 20 kV.

2.2. Synthesis of Gold Nanoparticles. Starch-stabilized gold nanoparticles were synthesized by modification of the procedure reported by Huang and coworker.[27] In a typical synthesis, 1.2 mL of an aqueous solution of $HAuCl_4·3H_2O$ (10 mmol dm^{-3}) was added to 10 mL of a starch solution (4 mg/mL), and the mixture was held at 55 °C for 2 h with constant stirring. The solution was then allowed to cool to room temperature. The color of the solution became red, indicating the formation of gold nanoparticles. The gold nanoparticles prepared by this method were found to be stable for a couple of weeks without any significant agglomeration or precipitation of the particles.

2.3. Synthesis of Fe_3O_4 Nanoparticles. Poly(ethylene glycol)-stabilized (PEG with hydroxyl end groups have been used, named PEG-13) iron oxide nanoparticles were synthesized by mixing a 1:2 molar ratio of Fe^{2+}/Fe^{3+} by following the method reported by Gillich et al.[28] In a typical synthesis, 1.99 g of $(NH_4)_2Fe(SO_4)_2·6H_2O$ and 5.41 g of $FeCl_3·6H_2O$ were dissolved in 50 mL of distilled water in a beaker. In a separate beaker, an aqueous NH_4OH (30% w/w) solution was prepared. After that, poly(ethylene glycol) (18.6 g) was added in a ratio of M/L = 1:10 (9.3 g each) to both the above solutions to get precursor solutions I and II, respectively. Then, precursor solution II was added to solution I dropwise under stirring at 40 °C. Just after the solutions were mixed, the color of the solution changed from light brown to black, indicating the formation of Fe_3O_4 nanoparticles. The stirring was continued for another 45 min. The precipitate so obtained was washed three times by centrifugation and redispersed in distilled water.

2.4. Synthesis of Au and Fe_3O_4 Nanoparticles-Decorated Composite Microcapsules. Nanoparticle-decorated composite microcapsules were prepared from starch-stabilized Au and PEG-stabilized Fe_3O_4 nanoparticles at a liquid–liquid interface via ligand cross-linking in the presence of terephthaloyl chloride (a well-known ligand cross-linker). In a typical method, 300 μL of terephthaloyl chloride (1.0 mmol dm^{-3}) in toluene was taken in a 2 mL centrifuge tube, and then 15 μL of an aqueous dispersion of each of Au (2.4 mmol dm^{-3}) and Fe_3O_4 (3.0 mmol dm^{-3}) nanoparticles was added. The reaction mixture was occasionally sonicated and vigorously shaken for 10 min. As a result, the dark toluene solution became colorless and the nanoparticle-stabilized Pickering emulsion droplets so formed settled at the bottom of the centrifuge tube. The droplets were washed three times and finally dispersed in fresh toluene for subsequent experiments.

3. RESULTS AND DISCUSSION

The absorption spectral features (all measured in the solid state for comparison) of Au, Fe_3O_4, and composite capsules are shown in Figure 1. The inset shows a digital photograph of the colloidal dispersion of the corresponding nanoparticles and the capsules. Gold nanoparticles exhibit an absorption spectrum

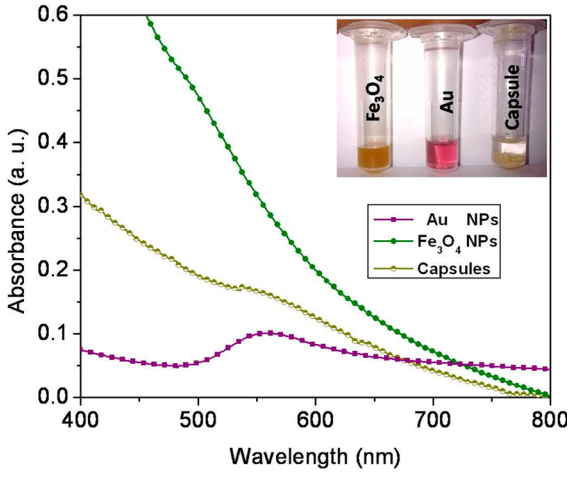

Figure 1. Absorption spectra (measured in the solid state) of Au NPs, Fe_3O_4 NPs, and composite capsules. The inset shows a digital photograph of the colloidal dispersion of the corresponding nanoparticles and the capsules.

dx.doi.org/10.1021/la5018054 | Langmuir 2014, 30, 10449−10455

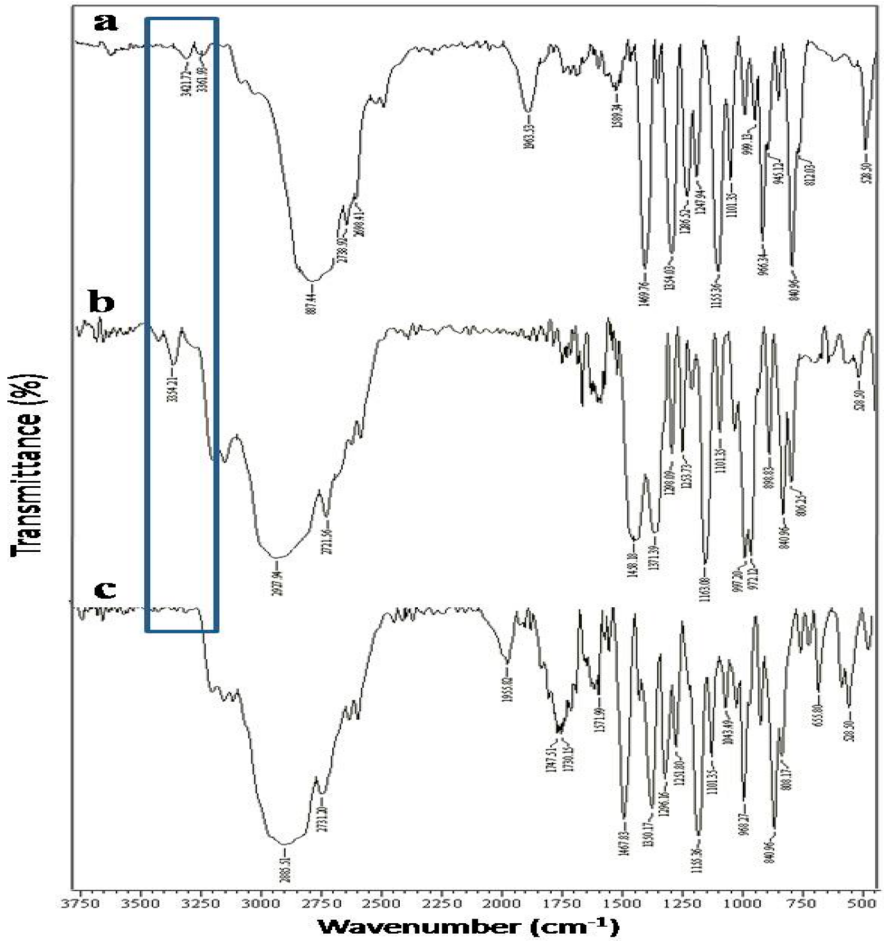

Figure 2. FTIR spectra of (a) poly(ethylene glycol)-stabilized Fe_3O_4 NPs, (b) starch-stabilized Au NPs, and (c) composite capsules.

Scheme 1. Schematic Description of the Au and Fe_3O_4 Nanoparticle-Decorated Composite Microcapsules Formed by Ligand Polymerization at the Water−Toluene Interface

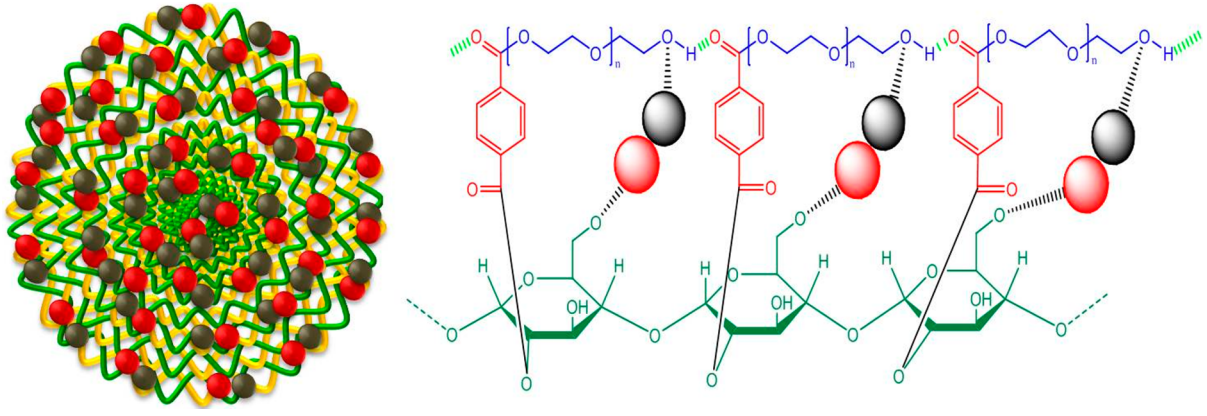

with a maximum at ca. 550 nm corresponding to the characteristic surface plasmon resonance of conduction electrons of the particles.[29] The broad absorption spectrum at longer wavelength could be attributed to the electromagnetic coupling effect among the gold nanoparticles in the solid state.[30] The electronic absorption spectrum of iron oxide nanoparticles shows three well-defined regions: the first portion below 500 nm, the second from 500 to 600 nm, and the third one finishing at 800 nm. The first portion is assigned to the allowed $O^{2-} \rightarrow Fe^{2+}$ and $O^{2-} \rightarrow Fe^{3+}$ charge-transfer transitions, and the last two can be reasonably related to d−d crystal-field transitions, $^3E_g(G) \leftarrow {}^3T_{1g}$, $^3A_{2g}(F) \leftarrow {}^3T_{1g}$, $^3A_{2g}(G) \leftarrow {}^3T_{1g}$, $^3T_{2g}(H) \leftarrow {}^3T_{1g}$, $^3T_{1g}(H) \leftarrow {}^3T_{1g}$, and $^3E_g(H) \leftarrow {}^3T_{1g}$, on octahedral Fe^{3+} species.[31,32] The spectrum of the capsules reveals the presence of both types of nanoparticles. The salient feature of physical significance is that the portion of the absorption band due to the charge-transfer transition of Fe_3O_4 vanishes due to interaction with the gold nanoparticles. This vanishing of the charge-transfer band is presumably due to chemical bonding or electron transfer to the

dx.doi.org/10.1021/la5018054 | Langmuir 2014, 30, 10449−10455

gold nanoparticles, as a result of the strong interaction between the Au and Fe_3O_4 nanoparticles in the capsules.[33]

The cross-linking between the ligands attached to the nanoparticle surface has been established by FTIR spectroscopic studies. Figure 2 shows the FTIR spectra of starch-stabilized Au NPs, PEG-stabilized Fe_3O_4 NPs, and composite capsules. Before polymerization, spectra of both starch and PEG exhibit peaks at about 3450 and 3550 cm^{-1}, respectively, corresponding to their respective −OH groups. Since −OH groups are residing in a hydrophobic pocket formed by the two adjacent polymers, the peak is very weak compared to the C−H peak.[34] Upon reaction with terephthaloyl chloride, both peaks are absent from the spectrum of the capsules, indicating successful cross-linking between ligands attached to the surfaces of both types of nanoparticles through the cross-linker, resulting in the appearance of a new ester peak at ∼1720 cm^{-1}. In other words, the disappearance of the two peaks and the appearance of the characteristic ester C−O stretching peak anticipates the formation of a polymerized network between the attached ligands around the droplet. Scheme 1 shows a schematic description of the organic−inorganic hybrid capsules formed by ligand polymerization. In this experiment, two types of nanoparticles have been cross-linked by joining the pendant hydroxyl groups of starch and PEG (viz., PEG-13) anchored to the gold and iron oxide nanoparticles, respectively; cross-linking (via ester linkage) occurs with two acyl chloride moieties of the terephthaloyl chloride molecule to form a rigid and amphiphilic network at the oil−water interface and stabilize the capsules. However, it is to be noted that after incorporating effective ligand coverage, both types of nanoparticles become dispersible in bulk liquid, i.e., the nanoparticles lose their interfacial activity; therefore, the origin of the nanoparticle surface activity is not essential to the creation of the capsules. It is observed that PEG-stabilized nanoparticles are soluble in both solvents. However, when these PEGylated particles react with the acyl chloride moiety of terephthaloyl chloride molecules for cross-linking, they become amphiphilic as the terephthaloyl chloride molecules become a part of the network which is insoluble in water.[35] Therefore, the droplets of the minor phase will get covered with ligand-stabilized nanoparticles that could also be cross-linked from the organic phase by reaction of the pendant hydroxyl groups of the ligands with terephthaloyl chloride.[35,36]

Figure 3 shows the optical microscope images of the capsules, as-prepared and dried under the dark-field condition of the microscope. The as-prepared capsules were transferred with a micropipette to the cavity of a glass slide and dispersed in toluene. The images of the as-prepared capsules (panel a) show that the capsules are spherical or nearly spherical with no observable fluctuations. The capsules exhibit relatively large

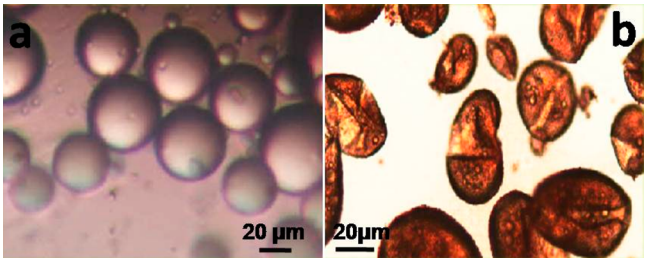

Figure 3. Optical microscope images of (a) as-prepared and (b) dried capsules.

sizes with a size distribution of ca. 20−40 μm and are likely to be hollow due to a clear outline of the sphere. The capsules do not exhibit any tendency to aggregation until these are dispersed in toluene as confirmed by optical microscopy. Upon drying under atmospheric condition on the cavity of a glass slide (panel b), the capsules shrink as a result of the crumpling of the colloidal shells of the capsules upon drying, indicating the robust nature of the capsule wall.[37]

Nanoparticles of Au- and Fe_3O_4-decorated composite capsules were drop-cast and subsequently dried on a silicon wafer for characterization by scanning electron microscopy. Representative SEM images of the capsules are presented in Figure 4. The SEM image (as-prepared capsules were drop-cast

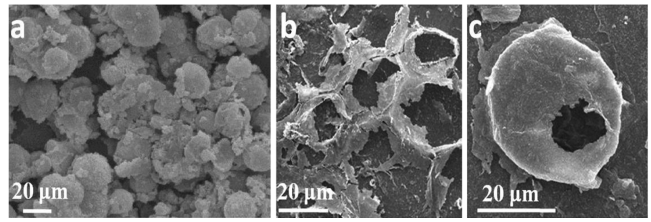

Figure 4. Scanning electron microscopy images of the (a) as-prepared and (b) dried capsules and (c) capsules with hollow interiors.

and subsequently dried on the silicon wafer) (panel a) illustrates the good spherical shape and the surface morphology of the capsules on the silicon wafer. Upon drying (capsules already dried under atmospheric condition were drop-cast on the silicon wafer) (panel b), the thin-film morphology and the membranous structure of the capsule shell are retained after drying, indicating successful cross-linking between the particles. At high magnification (as-prepared capsules were drop-cast and subsequently dried on the silicon wafer) (panel c), a hollow interior of the capsules is apparent, indicating that the nanoparticles are assembled only at the surface of the emulsion droplets. The hollow interior of the capsules can provide an ideal microcontainer for encapsulation and can control the diffusion of the active core ingredients across the capsule wall.[38]

Transmission electron micrographs of the individual gold and iron oxide nanoparticles and the composite capsules (as-prepared capsules were drop-cast and subsequently dried on the carbon-coated copper grid) are presented in Figure 5. It is

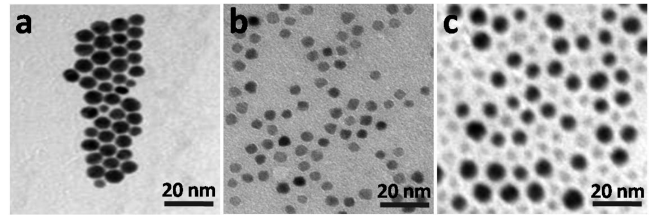

Figure 5. Transmission electron micrographs of the (a) Au, (b) Fe_3O_4, and (c) nanoparticle-decorated composite capsules.

observed that that the sizes of Au and Fe_3O_4 NPs are 10.0 ± 2.0 and 6.0 ± 0.7 nm, respectively. The image of the capsules shows interdigitated Au and Fe_3O_4 NPs which identify that the capsules are composed of shells of closely packed particles with liquidlike ordering. The interstitial space in these nanoparticle-based materials points to the possibility to provide ideal channels to restrict the diffusion of encapsulates through the capsule wall.

dx.doi.org/10.1021/la5018054 | *Langmuir* 2014, 30, 10449−10455

Figure 6 shows the magnetic behavior of the as-prepared capsules in the presence of an external magnetic field. In the absence of a magnetic field, capsules remain homogeneously distributed at the bottom of the beaker. When a magnetic bar is placed near the beaker, the attraction of the capsules in the presence of the magnetic field suggests that the capsules are magnetic in nature. Therefore, these systems can be manipulated using external magnetic fields, providing a convenient and gentle means of positioning the materials. The magnetic nature of the capsules could be exploited with a high application potential in materials science as well as in biological sciences.[36] The incorporation of gold nanoparticles adds plasmonic properties to the capsules, which can be exploited as a tool for drug delivery in living cells.[39] Nanoparticles absorb energy from a laser beam in the biologically friendly near-infrared region; the absorbed energy causes local heating and results in the disruption of the shells of the capsules and hence the release of the encapsulated material.[39]

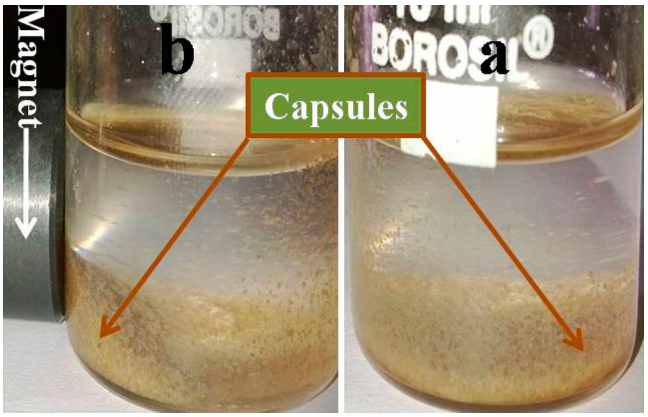

Figure 6. Digital camera photograph of the composite capsules in the (a) absence and (b) presence of a magnetic bar.

We have tried to elucidate the permeability of the composite microcapsules by encapsulating water-soluble fluorescent dyes of different molecular sizes (FITC and its two dextran conjugates, viz., FITC-D 40S and FITC-D 2000S) and subsequently allowing them to pass through the capsule wall. The FITC dye was selected because it has wide-ranging applications as an antibody and other probe labels for use in fluorescence microscopy, flow cytometry, and immunofluorescence-based assays.[40] Fluorescein isothiocyanate−dextran conjugates have been examined as a fluorescent probe for studying cell processes such as cell permeability, phagocytosis, and endocytosis and for studying the mechanism of biomolecular delivery.[41] The dye solution was encapsulated in the fluidic interior of the capsules by mixing an aqueous solution of dyes (1.0 mmol dm^{-3}) with the aqueous dispersion of the mixture of nanoparticle while preparing the capsules. The dye-impregnated capsules were washed three times with fresh toluene and transferred into distilled water in a cuvette, and the fluorescence was measured at different time intervals.

Figure 7 shows the molecular structure of FITC (panel a) and its dextran conjugates (panel b) and a schematic presentation of the release of the fluoroprobes from the dye-loaded capsules (panel c). Time-dependent fluorescence spectra ($\lambda_{ex} \approx 490$ nm) of the aqueous dispersion of the dye-released capsules were measured. As the capsules are of micrometer size, they remain at the bottom of the cuvette; the incident radiation passes through the solution of the cuvette; therefore, only the dye molecules coming out of the capsules into the bulk aqueous phase would be detected to fluoresce, but not those remaining inside the capsules. A plot of fluorescence intensity at 560 nm as a function of time for three different dye molecules is summarized in Figure 8. It is observed that in the case of FITC, the fluorescence intensity gradually increases with time, slowly increases for FITC-D 40S, and remains nearly

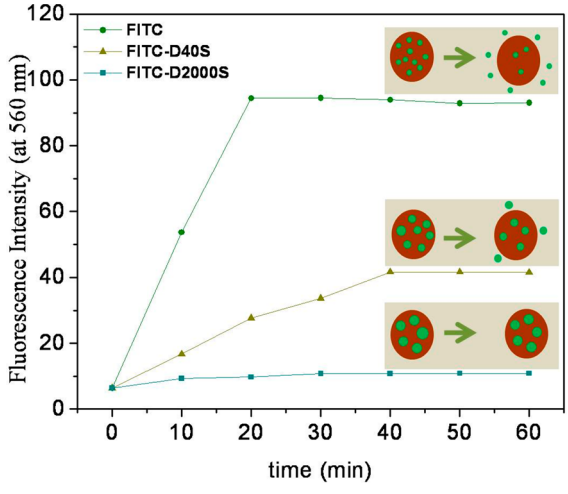

Figure 8. Plot of fluorescence intensity as a function of time during the release of the dye across the capsule wall. Insets show the schematic depiction of the release of the dye across the capsule wall.

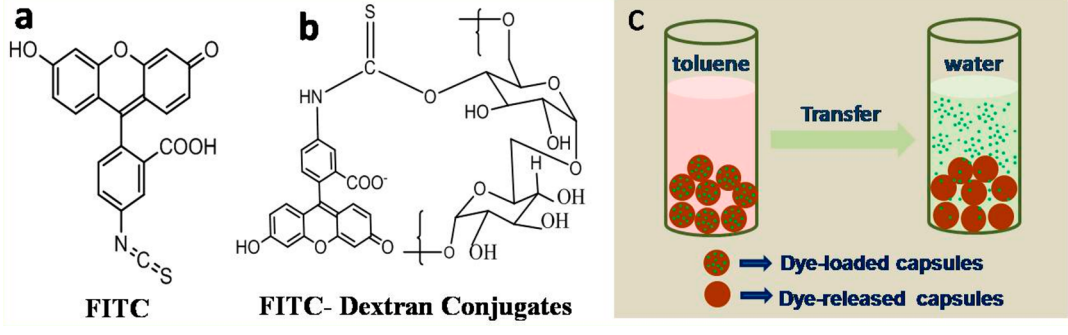

Figure 7. (a, b) Molecular structure of fluorescein isothocyanate and its dextran conjugates, respectively, and (c) schematic presentation of dye release upon transfer from toluene to aqueous solvent.

dx.doi.org/10.1021/la5018054 | *Langmuir* 2014, 30, 10449−10455

constant for FITC-D 2000S. It seems that the capsules, however, release FITC and FITC-D 40S but retain FITC-D 2000S, with no dye release observed over a period of 1 h. The hydrodynamic radii of FITC, FITC-D 40S, and FITC-D 2000S are 0.54, 3.7, and 9.4 nm, respectively.[42] From these observations, it can be inferred that FITC molecules are small enough to diffuse through the capsule shell due to the concentration gradient, FITC-D 40S molecules are neither small enough to pass easily through the capsule wall nor large enough for total retention, but FITC-D 2000S molecules are essentially not able to permeate the composite microcapsules as depicted schematically in the insets of Figure 8. It is assumed that the outside surface of the capsule is nonreactive with the dye molecules after they have been released from the capsules. Since the capsules were fabricated by performing interfacial cross-linking of the associated ligand molecules around the nanoparticles, their permeability is expected to be determined by the size of the interstices across the capsule wall.[43] The optical microscope images of the capsules have been seen before and after dye release, and it was observed that the capsules were not broken, suggesting that leakage was through diffusional loss of the dye molecules instead of capsule rupture.[44,45] Therefore, it could be concluded that the capsule shell acts as a semipermeable membrane exhibiting size-selectivity of the dye molecules during release across the capsule wall. In this diffusion process of the dye molecules through the nanoparticle-decorated capsules, it could be anticipated that the formation of multilayers of the capsules wall could significantly reduce the release rate.[46] It could therefore be suggested that at increased concentrations and low particle sizes, the capsule shell should be more consistent with the particles, thereby governing the slow release of the active substances across the capsule wall.

4. CONCLUSIONS

A simple and facile strategy has been developed for the synthesis of composite microcapsules with plasmonic and magnetic nanoparticles as building blocks by ligand cross-linking being effective at room temperature. These composite microcapsules illustrate permeation control for size-specific dye molecules across the capsule wall. Due to the presence of both the plasmonic and magnetic nature of the constituent nanoparticles, these capsules could be promising materials to explore in cancer imaging and therapy. Finally, the fabrication of nanoparticle capsules by this technique is general and could be extended to other nanoparticulate systems.

AUTHOR INFORMATION

Corresponding Author

*E-mail: sujit.kumar.ghosh@aus.ac.in.

Notes

The authors declare no competing financial interest.

ACKNOWLEDGMENTS

We gratefully acknowledge financial support from DST, New Delhi, India (project no. SR/FT/CS-68/2010).

REFERENCES

(1) Lasic, D. D. *Liposomes: Physics to Applications*; Elsevier: Amsterdam, 1993.

(2) Wilcox, D. L. *Hollow and Solid Spheres and Microspheres: Science and Technology Associated with Their Fabrication and Application*; Materials Research Society: Pittsburgh, PA, 1995; Vol. 372.

(3) Vriezema, D. M.; Aragones, M. C.; Elemans, J. A. A. W.; Cornelissen, J. J. L. M.; Rowan, A. E.; Nolte, R. J. M. Drug delivery using nanoparticle-stabilized nanocapsules. *Chem. Rev.* **2005**, *105*, 1445−1489.

(4) Pickering, S. U. CXCVI−Emulsions. *J. Chem. Soc. Trans.* **1907**, *91*, 2001−2021.

(5) Pieranski, P. Directing colloidal assembly at fluid interfaces. *Phys. Rev. Lett.* **1980**, *45*, 569−572.

(6) Wang, D.; Möhwald, H. Self-Assembly of nanoparticles by molecular recognition. *J. Mater. Chem.* **2004**, *14*, 459−468.

(7) Binder, W. H. Supramolecular assembly of nanoparticles at liquid−liquid interfaces. *Angew. Chem., Int. Ed.* **2005**, *44*, 5172−5175.

(8) Böker, A.; He, J.; Emrick, T.; Russell, T. P. Self-assembly of nanoparticles at interfaces. *Soft Matter* **2007**, *3*, 1231−1248.

(9) Binks, B. P. Particles as surfactants-similarities and differences. *Curr. Opin. Colloid Interface Sci.* **2002**, *7*, 21−24.

(10) Dahl, J. A.; Maddux, B. L.; Hutchison, J. E. Toward greener nanosynthesis. *Chem. Rev.* **2007**, *107*, 2228−2269.

(11) De Geest, B. G.; McShane, M. J.; Demeester, J.; De Smedt, S. C.; Hennink, W. E. Self-assembled structures: Properties and applications in solution. *J. Am. Chem. Soc.* **2008**, *130*, 14480−14482.

(12) Duan, H.; Wang, D.; Sobal, N. S.; Giersig, M.; Kurth, D. G.; Möhwald, H. Magnetic colloidosomes derived from nanoparticle interfacial self-assembly. *Nano Lett.* **2005**, *5*, 949−952.

(13) Koo, H. Y.; Chang, S. T.; Choi, W. S.; Park, J.-H.; Kim, D.-Y.; Velev, O. D. Emulsion-based synthesis of reversibly swellable, magnetic nanoparticle-embedded polymer microcapsules. *Chem. Mater.* **2006**, *18*, 3308−3313.

(14) Samanta, S.; Patra, D.; Subramani, C.; Ofir, Y.; Yesilbag, G.; Sanyal, A.; Rotello, V. M. Stable magnetic colloidosomes via click-mediated crosslinking of nanoparticles at water−oil interfaces. *Small* **2009**, *5*, 685−688.

(15) Shi, X.; Wang, S. H.; Swanson, S. D.; Ge, S.; Cao, Z.; Van Antwerp, M. E.; Landmark, K. J.; Baker, J. R., Jr. Dendrimer-functionalized shell-crosslinked iron oxide nanoparticles for *in vivo* magnetic resonance imaging of tumors. *Adv. Mater.* **2008**, *20*, 1671−1678.

(16) Zhou, J.; Qiao, X.; Binks, B. P.; Sun, K.; Bai, M.; Li, Y.; Liu, Y. Magnetic Pickering emulsions stabilized by Fe_3O_4 nanoparticles. *Langmuir* **2011**, *27*, 3308−3316.

(17) Hu, S. H.; Liao, B. J.; Chiang, C. S.; Chen, P. J.; Chen, I. W.; Chen, S. Y. Core-Shell nanocapsules stabilized by single-component polymer and nanoparticles for magneto-chemotherapy/hyperthermia with multiple drugs. *Adv. Mater.* **2012**, *17*, 3627−3632.

(18) Kong, S. D.; Choi, C.; Khamwannah, J.; Jin, S. Magnetically vectored delivery of cancer drug using remotely on−off switchable nano capsules. *IEEE Trans. Magn.* **2013**, *49*, 349−352.

(19) Gorin, D. A.; Portnov, S. A.; Inozemtseva, O. A.; Luklinska, Z.; Yashchenok, A. M.; Pavlov, A. M.; Skirtach, A. G.; Möhwald, H.; Sukhorukov, G. B. Magnetic/gold nanoparticle functionalized biocompatible microcapsules with sensitivity to laser irradiation. *Phys. Chem. Chem. Phys.* **2008**, *10*, 6899−6905.

(20) Yu, H.; Chen, M.; Rice, P. M.; Wang, S. X.; White, R. L.; Sun, S. Dumbbell-like bifunctional Au-Fe_3O_4 nanoparticles. *Nano Lett.* **2005**, *5*, 379−382.

(21) Costi, R.; Saunders, A. E.; Banin, U. Colloidal hybrid nanostructures: A new type of functional materials. *Angew. Chem., Int. Ed.* **2010**, *49*, 4878−4897.

(22) Lopes, G.; Vargas, J. M.; Sharma, S. K.; Béron, F.; Pirota, K. R.; Knobel, M.; Rettori, C.; Zysler, R. D. Ag-Fe_3O_4 dimer colloidal nanoparticles: synthesis and enhancement of magnetic properties. *J. Phys. Chem. C* **2010**, *114*, 10148−10152.

(23) Skirtach, A. G.; Javier, A. M.; Kreft, O.; Köhler, K.; Alberola, A. P.; Möhwald, H.; Parak, W. J.; Sukhorukov, G. B. Laser-induced release of encapsulated materials inside living cells. *Angew. Chem., Int. Ed.* **2006**, *118*, 4728−4733.

(24) Xu, C. J.; Wang, B. D.; Sun, S. H. Dumbbell-like Au-Fe_3O_4 nanoparticles for target-specific platin delivery. *J. Am. Chem. Soc.* **2009**, *131*, 4216−4217.

(25) Jiang, J.; Gu, H. W.; Shao, H. L.; Devlin, E.; Papaefthymiou, G. C.; Ying, J. Y. Bifunctional Fe_3O_4–Ag heterodimer nanoparticles for two-photon fluorescence imaging and magnetic manipulation. *Adv. Mater.* **2008**, *20*, 4403–4407.
(26) Choi, J. S.; Jun, Y. W.; Yeon, S. I.; Kim, H. C.; Shin, J. S.; Cheon, J. Biocompatible heterostructured nanoparticles for multimodal biological detection. *J. Am. Chem. Soc.* **2006**, *128*, 15982–15983.
(27) Huang, H.; Yang, X. Synthesis of polysaccharide-stabilized gold and silver nanoparticles: a green method. *Carbohydr. Res.* **2004**, *339*, 2627–2631.
(28) Gillich, T.; Acikgöz, C.; Isa, L.; Schlüter, A. D.; Spencer, N. D.; Textor, M. PEG-stabilized core-shell nanoparticles: impact of linear *versus* dendritic polymer shell architecture on colloidal properties and the reversibility of temperature-induced aggregation. *ACS Nano* **2013**, *22*, 316–329.
(29) Link, S.; El-Sayed, M. A. Spectral properties and relaxation dynamics of surface plasmon electronic oscillations in gold and silver nanodots and nanorods. *J. Phys. Chem. B* **1999**, *103*, 8410–8426.
(30) Ghosh, S. K.; Pal, T. Interparticle coupling effect on the surface plasmon resonance of gold nanoparticles: From theory to applications. *Chem. Rev.* **2007**, *107*, 4797–4862.
(31) Vázquez-Olmos, A.; Redón, R.; Fernández-Osorio, A. L.; Saniger, J. M. Room-temperature synthesis of Mn_3O_4 nanorods. *Appl. Phys. A: Mater. Sci. Process.* **2005**, *81*, 1131–1134.
(32) Kijlstra, W. S.; Poels, E. K.; Bliek, A.; Weckhuysen, B. M.; Schoonheydt, R. A. Characterization of Al_2O_3-supported manganese oxides by electron spin resonance and diffuse reflectance spectroscopy. *J. Phys. Chem. B* **1997**, *101*, 309–316.
(33) Kim, K. S.; Winograd, N. X-ray photoelectron spectroscopic binding energy shifts due to matrix in alloys and small supported metal particles. *Chem. Phys. Lett.* **1975**, *30*, 91–95.
(34) Hussain, S. T.; Iqbal, M.; Mazhar, M. Size control synthesis of starch capped-gold nanoparticles. *J. Nanopart. Res.* **2009**, *11*, 1383–1391.
(35) Glogowski, E.; Tangirala, R.; He, J.; Russell, T. P.; Emrick, T. Microcapsules of pegylated gold nanoparticles prepared by fluid–fluid interfacial assembly. *Nano Lett.* **2007**, *7*, 389–393.
(36) Arumugam, P.; Patra, D.; Samanta, B.; Agasti, S. S.; Subramani, C.; Rotello, V. M. Self-assembly and cross-linking of FePt nanoparticles at planar and colloidal liquid–liquid interfaces. *J. Am. Chem. Soc.* **2008**, *130*, 10046–10047.
(37) Rotello, V. M. *Nanoparticles: Building Blocks of Nanotechnology*; Springer: New York, 2004; Chapter 1, pp 1–28.
(38) Kievit, F. M.; Zhang, M. Surface engineering of iron oxide nanoparticles for targeted cancer therapy. *Acc. Chem. Res.* **2011**, *44*, 853–862.
(39) Chan, W. C. W., Ed.; *Bio-Applications of Nanoparticles*; Landes Bioscience: Austin, TX, 2007; Chapter 4, pp 48–56.
(40) Thorball, N. FITC-dextran tracers in microcirculatory and permeability studies using combined fluorescence stereo microscopy, fluorescence light microscopy and electron microscopy. *Histochemistry* **1981**, *71*, 209–233.
(41) Kim, T. H.; Park, T. G. Characterization of reservoir-type microcapsules made by the solvent exchange method. *Int. J. Pharm.* **2004**, *271*, 207–214.
(42) Ghosh, S. K.; Ali, M.; Chatterjee, H. Studies on the interaction of fluorescein isothiocyanate and its sugar analogues with cetyltrimethylammonium bromide. *Chem. Phys. Lett.* **2013**, *561–562*, 147–152.
(43) He, J.; Lin, X.; Chan, H.; Vukovic, L.; Král, P.; Jaeger, H. M. Diffusion and filtration properties of self-assembled gold nanocrystal membranes. *Nano Lett.* **2011**, *11*, 2430–2435.
(44) Liu, T.-Y.; Liu, K.-H.; Liu, D.-M.; Chen, S.-Y.; Chen, I.-W. Temperature-sensitive nanocapsules for controlled drug release caused by magnetically triggered structural disruption. *Adv. Funct. Mater.* **2008**, *18*, 1–8.
(45) Ritger, P. L.; Peppas, N. A. A simple equation for description of solute release II. Fickian and anomalous release from swellable devices. *J. Controlled Release* **1987**, *5*, 37–42.
(46) Emerich, D. F.; Thanos, C. G. The pinpoint promise of nanoparticle-based drug delivery and molecular diagnosis. *Biomol. Eng.* **2006**, *23*, 171–184.

CrystEngComm

PAPER

Water/*n*-heptane interface as a viable platform for the self-assembly of ZnO nanospheres to nanorods†

Cite this: *CrystEngComm*, 2014, **16**, 7696

Mohammed Ali, Hasimur Rahaman, Dewan S. Rahman, Surjatapa Nath and Sujit Kumar Ghosh*

Received 7th April 2014,
Accepted 5th June 2014

DOI: 10.1039/c4ce00728j

www.rsc.org/crystengcomm

The water/*n*-heptane interface has been exploited as a viable and selective platform for the transformation of quasi-spherical ZnO nanoparticles to nanorods, using an unconventional low precursor salt concentration under facile and benign reaction conditions. The transformation of nanospheres to nanorods has been characterised by absorption, fluorescence and Fourier transform infrared spectroscopy, X-ray diffraction and transmission electron microscopy. The mechanism of transformation to nanorods from the ultrasmall ZnO particles in the restricted environment provided by the liquid–liquid interface has been elucidated.

1. Introduction

In recent years, the self-assembly of nanoscale objects has paved the way towards a simple and general strategy to organise nanoparticles into higher order architectures.[1] Such processes require adequate stabilisation of the nanoparticles at interfaces with a high degree of organisational selectivity.[1,2] Amongst the three different approaches that are currently exploited to effect ordering of nanoparticles by the self-assembly processes, liquid–liquid interfaces offer an important alternative scaffold for colloidal crystallisation into higher ordered nanostructures.[2] A number of innovative approaches have been explored to engender interfacial ordering effects for the organisation of nanometer-size objects into both two and three dimensions, including membranes,[3] capsules,[4] core–shell structures,[5] heterodimeric alloyed nanostructures,[6] Janus particles,[7] and giant supramolecular assemblies[8] with distinct functionalities. Nanoobjects made with the semiconductor zinc oxide (ZnO) have attracted immense interest due to its direct wide band gap (3.37 eV), high exciton binding energy (60 meV) and the opportunity to vary its properties by morphological tuning.[9] One-dimensional semiconductor (ZnO) nanostructures (nanowires and nanorods) have attracted special interest due to their fascinating physical properties and potential applications in electronic and photonic devices.[9]

A variety of synthetic strategies have been adopted in the literature for the fabrication of ZnO nanorods, for example, high temperature physical evaporation,[10] micro-emulsion based hydrothermal process,[11] alcohol thermal process[12] and so on. Yin *et al.*[13] have reported the synthesis of ZnO quantum nanorods by thermal decomposition of zinc acetate (40 mM) in organic solvents in the presence of oleic acid at 286 °C for 1 h under N_2 flow. Wang and colleague[14] have designed the directed growth of ZnO nanorod arrays on a zinc substrate by the alkaline hydrolysis of zinc foils (15 × 15 × 0.25 mm^3) in the presence of cetyltrimethylammonium bromide loaded into a Teflon-lined stainless steel autoclave by heating at 160 °C for 20 h. Ho and co-authors[15] have developed a solution-based synthesis to grow highly ordered ZnO nanorod-like structures on selective areas of the substrate by heating zinc acetate (5–10 mM) at 90 °C for 8 h in a tightly sealed polypropylene screw cap tube. Guo *et al.*[16] reported the synthesis of ZnO nanorods by ripening the mixture of zinc acetate (50 mM) and potassium hydroxide in methanol at 70 °C, at least, for three days to achieve a narrow size distribution. The Weller group[17] have found that, in a methanolic solution, at a zinc acetate dihydrate concentration of below 10 mM, quasi-spherical particles are formed; whereas mainly nanorods are formed at ten times higher concentration of the precursor. In general, these synthetic methods are carried out with a high concentration of the precursor salt by forced hydrolysis in the presence or absence of a weak base. In this communication, we have found that the water/*n*-heptane interface could offer a viable platform for the self-assembly of ZnO nanodots to nanorods using an unconventional low precursor salt concentration (1.0 mM) under facile and benign reaction conditions.

Department of Chemistry, Assam University, Silchar-788011, India.
E-mail: sujit.kumar.ghosh@aus.ac.in; Fax: +91 3842 270802; Tel: +91 3842 270848

† Electronic supplementary information (ESI) available: Fluorescence spectra and TEM images. See DOI: 10.1039/c4ce00728j

2. Experimental section

2.1. Reagents and instruments

All the reagents used were of analytical reagent grade. Zinc(II) acetate dihydrate, $[Zn(OOCCH_3)_2{\cdot}2H_2O]$ and potassium hydroxide (KOH), were purchased from Sigma Aldrich and used as received. All the solvents *viz.* *n*-heptane, benzene, toluene, dichloromethane, cyclohexane and *o*-xylene were purchased from Sisco Research Laboratories and used without further purification. Double distilled water was used throughout the course of the investigation. The temperature was 298 ± 1 K during the experiments.

Absorption spectra were recorded on a Shimadzu UV 1601 digital spectrophotometer (Shimadzu, Japan) with the sample in a 1 cm quartz cuvette. Fluorescence spectra were recorded using a Perkin Elmer LS-45 spectrofluorometer (Perkin Elmer, UK). Fourier transform infrared (FTIR) spectra were recorded from pressed KBr pellets (in the range 400–4000 cm^{-1}) using a Shimadzu-FTIR Prestige-21 spectrophotometer. Transmission electron microscopy (TEM) measurements were performed on carbon-coated copper grids with a Zeiss CEM 902 operated at 200 kV. Powder X-ray diffraction (XRD) patterns were obtained using a D8 ADVANCE Bruker AXS X-ray diffractometer with CuK_α radiation (λ = 1.4506 Å); data were collected at a scan rate of 0.5° min^{-1} in the range of 10°–80°.

2.2. Synthesis of ZnO nanomaterials

In a typical experiment, an amount of 0.055 g zinc acetate dihydrate was dissolved in 25 mL of solvent mixture (water : *n*-heptane = 9 : 1) in a double-necked round-bottom flask by refluxing in a water bath at 65 °C. After 15 min, 13.5 mL aqueous KOH solution (0.1 mM) was added to the mixture and the refluxing was continued for another 2 h. It was seen that, initially, a faint yellow colouration appeared that slowly transformed to curdy white, indicating progressive transformation of the nuclei into larger particles.[11] Finally, the mixture was cooled to room temperature and stored in the dark.

3. Results and discussion

The progressive transformation of the ultrasmall ZnO particles into larger aggregates has been studied by UV-vis absorption, fluorescence and Fourier transform infrared (FTIR) spectroscopy, X-ray diffraction (XRD) and transmission electron microscopy (TEM). Fig. 1 presents the absorption spectra, showing the time evolution of the primarily formed ZnO particles into larger aggregates and the fluorescence spectra of the finally formed particles synthesised at the water/*n*-heptane interface at different time intervals. At the beginning, the absorption spectrum shows two maxima, one at 219 nm (5.66 eV) and the other at 265 nm (4.68 eV), which are characteristic of spherical ZnO nanoparticles. In the case of semiconductor nanoparticles, the Fermi energy level lies in between the valence and conduction band, which is comprised of discrete energy states due to strong electron confinement. These two peaks arise due to the excitonic

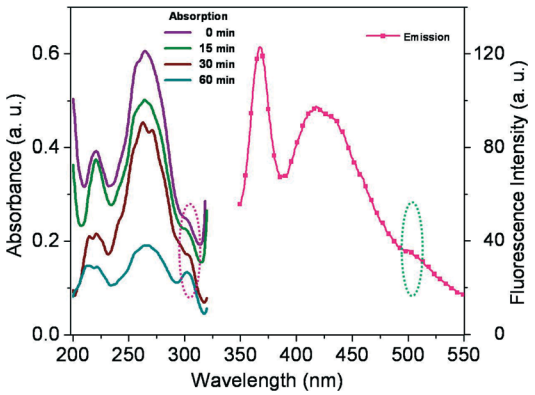

Fig. 1 Absorbance and fluorescence spectra showing the evolution of ZnO nanospheres to nanorods.

transitions between the trapped energy states situated within the confinement region.[18] The sizes of the intervening gaps are correlated with the band structure, which again depends on the size of the nanoparticles, on the basis of the interaction with the confined electrons among the lattice points. The optical band edge bears the characteristic electronic transition energy taking place to promote the electrons to the energy states in the conduction band from the valence band, including excitonic effects. As the time progresses, both the peaks decrease in intensity and a new peak at 302 nm (4.11 eV) develops, indicating the gradual transformation of ZnO nanospheres to nanorods.[16] The fluorescence spectrum (λ_{ex} ~ 302 nm) of the finally formed ZnO particles exhibits a narrow emission band at 379 nm (3.27 eV) that is attributed to the radiative recombination of a hole in the valence band and an electron in the conduction band (excitonic emission).[16] In addition, traces of two emission peaks at *ca.* 416 nm (2.98 eV) and 434 nm (2.86 eV) are seen that could be attributed to the presence of multiple surface defects in the ZnO nanorods.[19] The absorption and fluorescence spectra, thus, indicate the progressive transformation of the ZnO nanospheres to nanorods.

Fig. 2 shows the corresponding TEM images of the ZnO particles at the beginning and end of the reaction. It is seen that the initial particles are quasi-spherical in nature with average particle sizes of 3–5 nm, while the rod-shaped particles are *ca.* 100–200 nm and 15–20 nm in length and diameter, respectively. The corresponding selected area electron

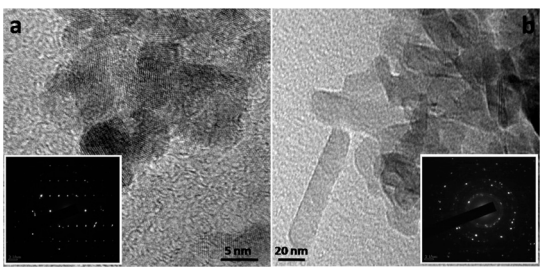

Fig. 2 Representative TEM images of ZnO particles at the (a) beginning and (b) end of the reaction. Insets show the corresponding selected area electron diffraction patterns of the ZnO nanostructures.

diffraction patterns (shown in the inset) reveal the appearance of polycrystalline-like diffraction, which is consistent with reflections (100), (002), (101), (102) and (110), corresponding to the hexagonal wurtzite phase of ZnO particles, indicating that the nanorod is an ordered assembly of small nanocrystal sub-units without crystallographic orientation.[20]

Detailed TEM investigations during the formation of the nanorods are presented in Fig. 3. At low magnification, aggregated quasi-spherical particles are seen (panel a) and these subsequently form pearl-chain-like structures (panel b). It could be recognised that the particles are epitaxially fused together, and bottlenecks between the adjacent attachments are seen along the *c*-axis (002), but laterally oriented attachment parallel to the *c*-axis is also evident (panel c). In some cases, it is apparent that the individual particles are aligned like a wall, where the second layer of bricks is just starting to be put on the particles that are still visible. Therefore, it is evident that the nanorods are formed by coalescence through the 'oriented attachment' of quasi-spherical particles. This model of transformation of ZnO nanospheres to nanorods has been evidenced by the Weller group.[17] Oriented attachment has, previously, been proposed by other authors during the crystal growth of iron oxide, TiO_2 with sizes of a few nm and for micrometer sized ZnO particles during the formation of rod-like ZnO microcystals.[21–23]

Fig. 4 shows the high resolution TEM images of single ZnO nanorods with various magnifications. It is seen that the lattice planes of the depicted nanorods are almost perfectly aligned, with a lattice fringe of 0.26 nm consistent with the d_{002} spacing of wurtzite ZnO nanostructures.[24] Moreover, it could be recognised that the lattice planes go straight through the contact areas of the small spherical nanocrystals.

Fig. 5 shows the FTIR spectra of growing ZnO nanostructures at different time intervals. With increasing reflux time, it is seen that a peak at *ca.* 458 cm^{-1}, assigned to the stretching vibration of Zn–O bonds, is sharpening with time, indicating the crystallization of ZnO into higher order architectures.[23] Moreover, other peaks at *ca.* 805, 853 and 863 cm^{-1} exhibit similar trends with increasing reflux time.[25] In addition, strong absorption at 3442 cm^{-1} and weak absorptions around the 2800 to 3000 cm^{-1} region reveal the stretching vibrations of O–H and C–H, respectively. The absorption peak at 1104 cm^{-1} corresponds to the C–OH stretching and O–H bending vibrations, whereas the bands at 1383, 1577, and 1630 cm^{-1} correspond to C–O (hydroxyl, ester, or ether) stretching and O–H bending vibrations.[26] Therefore, it could be conceived that the dominant growth mechanism of ZnO nanorods is mainly the oriented attachment mechanism. The concomitant appearance of other bands indicates the presence of organic residues on the surface of the nanospheres that remain even after the formation of nanorods.

X-ray diffractograms of as-prepared ZnO samples with various reflux times are shown in Fig. 6. All patterns could be indexed to the pure hexagonal phase of Zn with a space group of C_{6v}^4 and cell constants a = 3.25 Å, and c = 5.21 Å (JCPDS card no.: 76-0704), which suggests that the product comprises ZnO nanocrystals with the wurtzite structure.[27] An increase in refluxing time increases the relative intensities of the (002) diffraction line, which is consistent with the rod formation along the *c*-axis of the particles.[24]

To elucidate the mechanism of transformation of ZnO nanospheres to nanorods at the liquid–liquid interface, a series of experiments was carried out. It is noted that the transformation to nanorods does not occur at the prescribed low precursor concentration in the presence of polar solvents, consistent with earlier observations.[17] The formation of the nanorods was tried in the presence of six water-immiscible solvents *viz.* cyclohexane, *n*-heptane, benzene, toluene, *o*-xylene and dichloromethane, and the fluorescence spectra (λ_{ex} ~ 302 nm) of the finally formed particles were measured (ESI† Fig. SI 1). The appearance of a new band at 503 nm only in the presence of *n*-heptane made us curious about the uniqueness of the morphology of the particles formed at the water/*n*-heptane interface. The TEM images of the particles formed in the presence of two other representative solvents, *viz.* dichloromethane and cyclohexane, are shown (ESI† Fig. SI 2). The transformation of the quasi-spherical particles to rods was not seen in any of these solvents. It is now well-established in the literature that the formation of the nanorods requires anisotropic crystal growth, based on the surface and attachment energies of various crystallographic planes.[17,21–23] When the present experiment is carried out in the absence of organic solvent, keeping all other experimental conditions unaltered, there is formation of ultrasmall ZnO nanoparticles. Therefore, it could be conceived that water/*n*-heptane interfacial tension offers the requisite restricted environment for the oriented attachment of the nanospheres to form nanorods. The composition of the solvent also plays a role for the transformation of nanospheres to nanorods. The fluorescence spectra obtained by varying the water/*n*-heptane composition are shown in ESI Fig. SI 3.† It is seen that a new

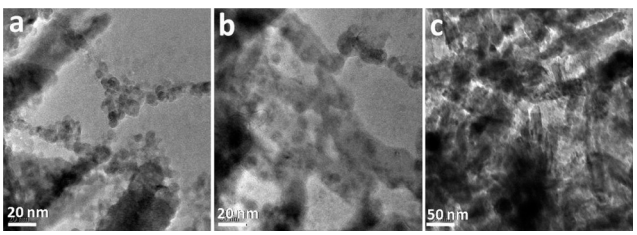

Fig. 3 TEM investigations during the formation of nanorods (a) 15, (b) 30 and (c) 45 min of reflux.

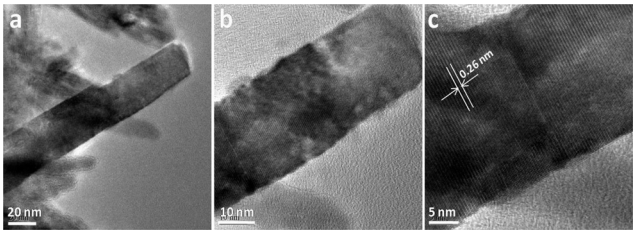

Fig. 4 TEM images of ZnO nanorods with increasing magnifications.

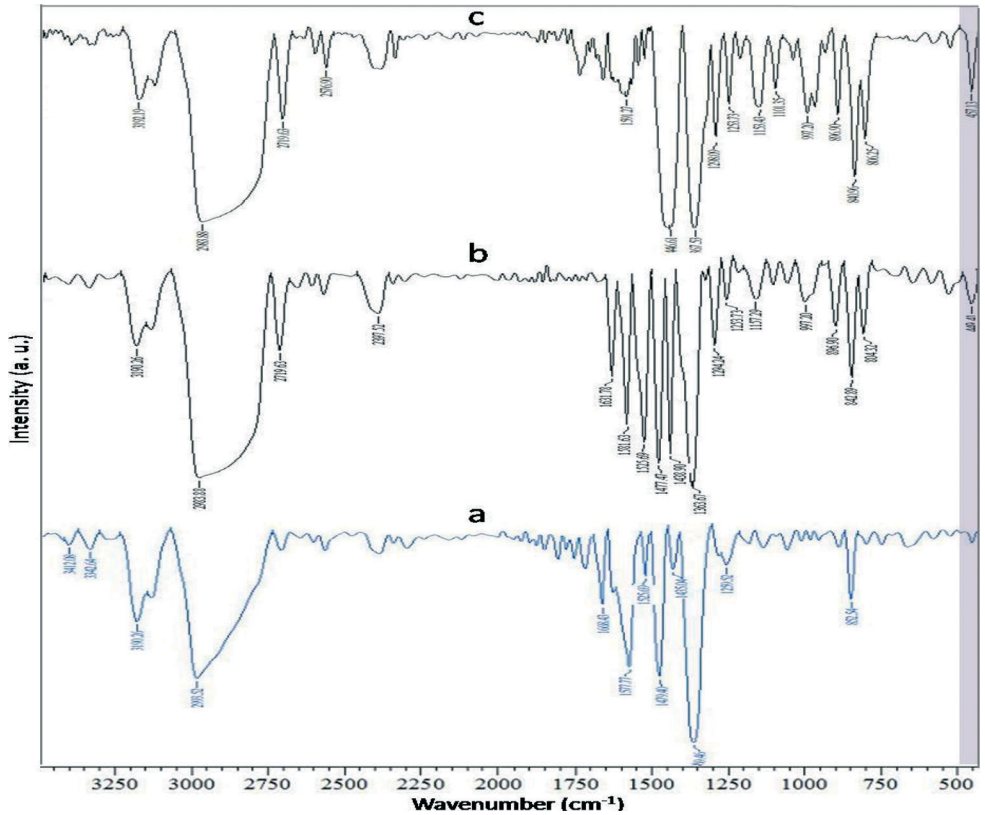

Fig. 5 FTIR spectra taken during the transformation of ZnO nanospheres to nanorods after (a) 0, (b) 30 and (c) 90 min of refluxing. The shaded area indicates the area of interest.

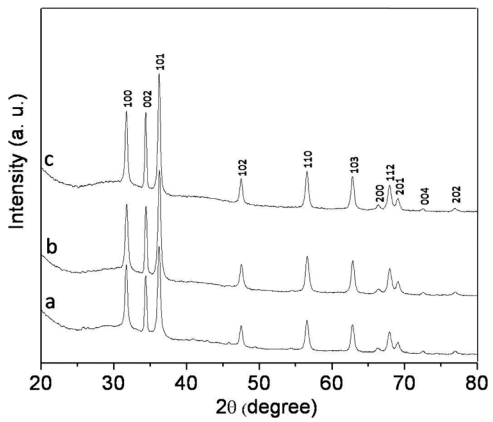

Fig. 6 X-ray diffractograms of the transformation of ZnO nanospheres to nanorods (a) 30 min, (b) 1 h and (c) 2 h of reflux.

band appears at 503 nm only in the presence of *n*-heptane at a volume ratio of water : *n*-heptane = 9 : 1; at a volume ratio above or below, the appearance of no such band is observed. Therefore, it could be concluded that formation of the nanorods is favoured at an optimum composition of the water and *n*-heptane mixture. It is now well established in the literature that a liquid–liquid interface is a non-homogeneous region, having a thickness of the order of a few nanometers.[28] The interface between two immiscible liquids, thus, offers an important scaffold for the chemical manipulation and self-assembly of the nanocrystals.[29] The interfacial tension at the water/*n*-heptane interface is dependent upon solvent composition. Therefore, it is manifested that, while the liquid–liquid interface offers a viable platform, the observed assembly is the result of specific interparticle interactions bringing about the transformation to nanorods. The attachment does not occur at room temperature, pointing out that a moderately higher temperature (65 °C; below the boiling point of *n*-heptane, 98.42 °C) helps to tailor the fusion of the particles. When two ZnO building blocks come together, the capillary forces between them facilitate the solvent removal and strengthen the agglomerate by van der Waals' forces. Finally, with an increase in reaction time, directed self-assembly of the oriented nanocrystallites and subsequent fusion lead to the formation of ZnO one-dimensional nanorods.[30] Therefore, on the basis of the above experimental results, a plausible mechanism for the transformation of ZnO nanospheres to nanorods through the oriented attachment of the ultrasmall particles could be developed, as depicted in Scheme 1.

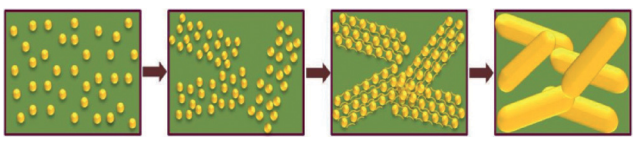

Scheme 1 Schematic presentation of the formation of nanorods from nanospheres.

4. Conclusions

A liquid–liquid interface has been exploited as a viable platform for the oriented attachment of quasi-spherical ZnO nanoparticles to form single crystalline nanorods under the prescribed reaction conditions. The formation of ZnO nanorods could be achieved at a very low concentration of the precursor in a restricted environment created by a particular composition of polar/non-polar liquid pairs. Incidentally, the transformation occurs selectively at the water/*n*-heptane interface, offering production of the nanorods under environmentally benign conditions.

Acknowledgements

We gratefully acknowledge financial support from DST, New Delhi (project no.: SR/FT/CS-68/2010).

Notes and references

1 E. Katz, A. N. Shipway and I. Willner, in *Nanoscale Materials*, ed. L. M. Liz-Marzan and V. P. Kamat, Kluwer, Norwell, 2003, pp. 317–343.
2 W. H. Binder, *Angew. Chem., Int. Ed.*, 2005, **44**, 5172–5175.
3 Y. Lin, H. Skaff, A. Böker, A. D. Dinsmore, T. Emrick and T. P. Russell, *J. Am. Chem. Soc.*, 2003, **125**, 12690–12691.
4 H. Duan, D. Wang, D. G. Kurth and H. Möhwald, *Angew. Chem., Int. Ed.*, 2004, **43**, 5639–5642.
5 Z. Niu, J. He, T. P. Russel and Q. Wang, *Angew. Chem., Int. Ed.*, 2010, **49**, 10052–10066.
6 H. Gu, Z. Yang, J. Gao, C. K. Chang and B. Xu, *J. Am. Chem. Soc.*, 2005, **127**, 34–35.
7 A. H. Gröschel, A. Walther, T. I. Löbling, J. Schmelz, A. Hanisch, H. Schmalz and A. H. E. Müller, *J. Am. Chem. Soc.*, 2012, **134**, 13850–13860.
8 M. Ali, S. K. Pal, H. Rahaman and S. K. Ghosh, *Soft Matter*, 2014, **10**, 2767–2774.
9 Z. L. Wang, *Appl. Phys. A: Mater. Sci. Process.*, 2007, **88**, 7–15.
10 Y. W. Wang, L. D. Zhang, D. J. Wang, X. S. Peng, Z. Q. Chu and C. H. Liang, *J. Cryst. Growth*, 2002, **234**, 171–175.
11 J. Zhang, L. D. Sun, H. Y. Pan, C. S. Liao and C. H. Yan, *New J. Chem.*, 2002, **26**, 33–34.
12 J. B. Cheng, X. B. Zhang, X. Y. Tao, H. M. Lu, Z. Q. Luo and F. Liu, *J. Phys. Chem. B*, 2006, **110**, 10348–10353.
13 M. Yin, Y. Gu, I. L. Kuskovsky, T. Andelman, Y. Zhu, G. F. Neumark and S. O'Brien, *J. Am. Chem. Soc.*, 2004, **126**, 6206–6207.
14 D. Wang and C. Song, *J. Phys. Chem. B*, 2005, **109**, 12697–12700.
15 C. H. Wang, A. S. W. Wong and G. W. Ho, *Langmuir*, 2007, **23**, 11960–11963.
16 Y. Guo, X. Cao, X. Lan, C. Zhao, X. Xue and Y. Song, *J. Phys. Chem. C*, 2008, **112**, 8832–8838.
17 C. Pacholski, A. Kornowski and H. Weller, *Angew. Chem., Int. Ed.*, 2002, **41**, 1188–1191.
18 A. P. Alivisatos, *Science*, 1996, **271**, 933–937.
19 M. L. Kahn, T. Cardinal, B. Bousquet, M. Monge, V. Jubera and B. Chaudret, *ChemPhysChem*, 2006, **7**, 2392–2397.
20 M. Y. Ge, H. P. Wu, L. Niu, J. F. Liu, S. Y. Chen, P. Y. Shen, Y. W. Zeng, Y. W. Wang, G. Q. Zhang and J. Z. Jiang, *J. Cryst. Growth*, 2007, **305**, 162–166.
21 J. F. Banfield, S. A. Welch, H. Zhang, T. T. Ebert and R. L. Penn, *Science*, 2000, **289**, 751–754.
22 A. Chemseddine and T. Moritz, *Eur. J. Inorg. Chem.*, 1999, 235–245.
23 M. Andres Verges, A. Mifsud and C. J. Serena, *J. Chem. Soc., Faraday Trans.*, 1990, **86**, 959–963.
24 D. Krishnan and T. Pradeep, *J. Cryst. Growth*, 2009, **311**, 3889–3897.
25 K. M. Joshi and V. S. Shrivastava, *Appl. Nanosci.*, 2011, **1**, 147–155.
26 M. Sevilla and A. B. Fuertes, *Chem. – Eur. J.*, 2009, **15**, 4195–4203.
27 M. Goano, F. Bertazzi, M. Penna and E. Bellotti, *J. Appl. Phys.*, 2007, **102**, 083709–083719.
28 A. Böker, J. He, T. Emrick and T. P. Russell, *Soft Matter*, 2007, **3**, 1231–1248.
29 D. Nykypanchuk, M. M. Maye, D. van der Lelie and O. Gang, *Nature*, 2008, **451**, 549–552.
30 M. Fernández-Garcia and J. A. Rodriguez, in *Nanomaterials: Inorganic and Bioinorganic Perspectives*, ed. C. M. Lukehart and R. A. Scott, John Wiley & Sons, West Sussex, UK, 2008, p. 453.

Soft Matter

PAPER

Interfacial assembly of ZnO quantum dots into giant supramolecular architectures†

Cite this: *Soft Matter*, 2014, **10**, 2767

Mohammed Ali, Sudip Kumar Pal, Hasimur Rahaman and Sujit Kumar Ghosh*

Received 8th October 2013
Accepted 6th January 2014

DOI: 10.1039/c3sm52610k

www.rsc.org/softmatter

Para-aminobenzoic acid (PABA) stabilised zinc oxide (ZnO) quantum dots (QDs) have been synthesised by refluxing zinc acetate dihydrate in methanol under alkaline condition and re-dispersed into water by centrifugation. Aqueous dispersion of PABA-stabilised ZnO QDs was taken with seven different organic solvents in test tubes and subjected to diazo reaction under specified conditions. It was seen that the quantum dots assembled into diverse superstructures depending on the nature of the immiscible solvent at the aqueous–organic interface. The assemblies so obtained have been characterised by energy dispersive X-ray (EDX) analysis, Fourier transform infrared (FTIR), fluorescence and Raman spectroscopy, X-ray diffraction (XRD) and thermogravimetric analysis (TGA), optical, fluorescence and scanning electron microscopic (SEM) images. It has been observed that the ensuing supramolecular assemblies exhibit significant electrical conductivity and photoluminescence properties.

1. Introduction

In recent years, self-assembly is a powerful strategy for creating hierarchical assemblies that have enticed researchers due to their significant scientific and potential technological applications.[1] Amongst the three different approaches currently explored to affect ordering of nanoparticles by self-assembly processes,[2] liquid–liquid interfaces offer an important alternative scaffold for the organisation of nanoscale substances into supramolecular assemblies.[3] While the nanoparticles possess specific functionalities, the attached ligands can be tuned to tailor interactions with the surroundings. Therefore, the interplay of self-organisation of the stabilising ligand shell with the functionality of inorganic nanomaterials has commenced as an effective approach to fabricate inorganic–organic hybrid assemblies. A number of innovative approaches have been explored to engender interfacial ordering effects for the organisation of nanometer-size objects into both two and three dimensions, including membranes,[4] capsules,[5] core–shell structures,[6] heterodimeric alloyed nanostructures[7] and Janus particles[8] with distinct functionalities.

Semiconductor nanoparticles have gained continuous scientific interest because of their unique quantum nature, which changes the material solid-state properties.[9] Due to quantum confinement, these nanomaterials display novel optical and transport properties which have great potential for prospective optoelectronic applications.[10] Zinc oxide is a IIb–VI compound semiconductor with direct wide band gap (~3.37 eV)[11] that displays high optical transparency and luminescent properties in the near ultraviolet and the visible regions.[12] The high exciton binding energy of ZnO (~60 meV) would allow for excitonic transitions even at room temperature, which could mean high radiative recombination efficiency for spontaneous emission as well as a lower threshold voltage for laser emission.[13] Moreover, ZnO has good thermal and chemical stability, which make the nanostructures of this material suitable for stable device applications.[14] This material has been considered a promising material for many applications, such as a transparent conductive contact, thin-film gas sensor, varistor, solar cell, luminescent material, surface electroacoustic wave device, heterojunction laser diode, ultraviolet laser and others.[15] Furthermore, the varieties of configurational architectures available for ZnO in the nanoscale[16,17] assure the conditions for formation of a richest microstructural diversity.[18] Therefore, the fabrication of hierarchical assemblies of ZnO has attracted critical importance to the development of functional nanodevices.[19]

In this article, we demonstrate interface-mediated unprecedented superstructures of ZnO quantum dots (2 ± 0.3 nm) exploring the diazo reaction as a cross-linking strategy. It is seen that the quantum dots assembled into submicrometer-, micrometer- and millimeter-sized supramolecular assemblies. Morphological variation of hierarchical assemblies could be envisaged under ambient conditions only by proper choice of the immiscible liquid pairs. The resultant organic–inorganic hybrid assemblies have been characterised by Fourier transform infrared, fluorescence and Raman spectroscopy, X-ray diffraction and thermogravimetric analysis, optical, fluorescence and scanning electron microscopic images. The electrical

Department of Chemistry, Assam University, Silchar-788011, India. E-mail: sujitkchem@gmail.com

† Electronic supplementary information (ESI) available. See DOI: 10.1039/c3sm52610k

conductivity and photoluminescence properties of the ensuing supramolecular assemblies have been elucidated.

2. Experimental

2.1. Reagents and instruments

All the reagents used were of analytical reagent grade. Zinc acetate dihydrate ($Zn(OOCCH_3)_2 \cdot 2H_2O$) (Aldrich) and *para*-aminobenzoic acid (PABA) (Merck, India), potassium hydroxide (S. D. Fine Chemicals, India), sodium nitrite (Merck, India) and hydrochloric acid (Qualigens' Fine Chemicals) were used as received. All the solvents were purchased from Sisco Research Laboratories and were used without further purification. Double distilled water was used throughout the course of the investigation. The temperature was 298 ± 1 K for all experiments.

Absorption spectra were recorded in a Shimadzu UV-1601 digital spectrophotometer (Shimadzu, Japan) taking the sample in a 1 cm well-stoppered quartz cuvette. Fluorescence spectra were recorded with a Shimadzu RF-5301 spectrofluorimeter (Shimadzu, Japan) equipped with a 9.9 W xenon flash lamp and a photomultiplier tube with S-20 spectral response. Transmission electron microscopy (TEM) was carried out on a JEOL JEM 2100 microscope with a magnification of 200 kV. Samples were prepared by placing a drop of solution on a carbon coated copper grid. The spectrofluorimeter was linked to a personal computer and utilised the RF-5301PC software package for data collection and processing. SEM images were recorded by using a JEOL (JSM-6360) Zeiss 1530 Gemini instrument equipped with a field emission cathode with a lateral resolution of approximately 3 nm and acceleration voltage 3 kV after sputtering the sample on a silicon wafer with carbon (approx. 6 nm). Thin films were prepared by drop-coating from the methanolic solutions of the respective samples onto silicon wafers. Energy dispersive X-ray (EDX) analysis was performed on a LEO 1530 field emission scanning electron microscope using an X-ray detector. An epoxy resin (EpoFix kit, Struers) was used to prepare specimens for cross-sectional SEM imaging. Ultrathin sections (50–70 nm in thickness) of the composite particles were cut with an Ultracut E Reichert-Jung microtome prepared at room temperature using a diamond knife (Drukker) and dropped on a silicon wafer by using a loop. Fourier transform infrared (FTIR) spectra were recorded in the form of pressed KBr pellets in the range (400–4000 cm^{-1}) on a Shimadzu-FTIR Prestige-21 spectrophotometer. The membrane was observed by optical microscope (Olympus BX 61) equipped with a high resolution DP70 digital charge coupled device (CCD) camera and images were processed using Aldus Photostyler 3.0 software. Fluorescence microscopic images of the membrane were recorded in a Zeiss fluorescence microscope (excitation: 276 nm, detection: 603 nm). The powder X-ray diffraction patterns were obtained using a D8 ADVANCE BROKERaxs X-ray Diffractometer with CuK_α radiation ($\lambda = 1.4506$ Å); data were collected at a scan rate of 0.5° min^{-1} in the range of 10°–80°. Thermogravimetric analysis was carried out on a Perkin–Elmer STA 6000 with the sample amount of 10 mg. The measurements were performed under nitrogen with heating from 30–800 °C (rate: 10 °C min^{-1}) and then, maintained at 800 °C for half an hour. Before TGA measurements, the samples were dried overnight in vacuum oven at 50 °C. Raman scattering measurements are carried out on silicon substrate in backscattering geometry using a fiber-coupled micro-Raman spectrometer equipped with 488 nm (2.55 eV) of 5 mW air cooled Ar^+ laser as the excitation light source, a spectrometer (model TRIAX550, JY) and a CCD detector. Electron transport in a thin film of each assembly was measured using an electrode geometry in which the conductivity was measured between two contacts which are separated by a narrow gap bridged by the material of interest. The electrical conductivity of the samples was measured over the temperature range of 300–373 K at an interval of 10 K by conventional multimeter.

2.2. Synthesis of *para*-aminobenzoic acid-stabilised zinc oxide nanoparticles

The ZnO nanoparticles were synthesised in a one-pot reaction using methanol as the solvent.[20] An aliquot of 0.055 g zinc acetate dihydrate was dissolved in 25 mL of methanol in a double-necked round-bottom flask by heating the mixture on a water bath at 45 °C. After dissolving zinc acetate, 1.545 g *para*-aminobenzoic acid was added to the solution and the reaction mixture was distilled at 45 °C for 30 min. Subsequently, the temperature of distillation was increased to 60 °C and 0.5 g KOH dissolved in 13.5 mL of methanol was added into the solution instantaneously. The distillation was continued for another 2 h and slowly a yellow colour developed in the solution indicating the formation of ZnO nanoparticles. Then, the water bath was removed and the mixture was stirred for 12 h at room temperature. The PABA-functionalised ZnO nanoparticles so obtained were retrieved from methanol by centrifugation at 13 000 rpm for 1 min and were subsequently re-dispersed into water. The ZnO nanoparticles prepared by this method are stable for a couple of weeks and can be stored in the dark for several days without any significant agglomeration or precipitation of the particles. A schematic presentation showing the formation of ZnO nanoparticles is depicted in ESI 1.† The transmission electron micrograph (particle diameter: 2 ± 0.3 nm) and selected area electron diffraction pattern of the ZnO particles are presented in ESI 2.† The particles formed by this method were subjected to diazo reaction for designing the hierarchical assemblies.

2.3. Synthesis of self-assembled zinc oxide nanoparticles at the liquid–liquid interface

An aqueous dispersion of 2 mL of PABA-stabilised ZnO QDs (10 mM) was mixed with 2 mL of the organic solvent (seven different solvents were separately employed) in a test tube. Now, the mixture was cooled in ice-bath and an aliquot of $NaNO_2$ (aq.)/dil. HCl at 0–5 °C was added into the test tube and shaken vigorously. It was seen that the nanoparticles possess a tendency to leave the aqueous phase and selectively reside at the interface (do not diffuse into the organic phase), forming assembled structures.

3. Results and discussion

The fluorescence microscopic images of the resultant assemblies in seven different solvents are shown in Fig. 1. The assemblies so formed were collected from the interface by micropipette and suspended into the respective organic solvents on a glass slide. It is observed that ultrasmall ZnO particles are assembled into variable architectures (a–g) depending upon the nature of the solvents. In *n*-hexane, toluene and dichloromethane, bamboo-shaped structures are formed while the width, noticeably, changes with the solvent. Arrayed needle-like structures are also created, the width of the needle being sharper in cyclohexane compared with benzene. Whilst ellipsoid capsules evolve in chloroform, a nanoparticle-decorated membrane is seen using CCl_4 as the solvent. The slight crumpling of the morphology of the membrane may result from shear stresses during manipulation with the micropipette. The observation of structurally intact supramolecular assemblies for all solvents indicates that the PABA molecules attached to the ZnO nanoparticles are cross-linked *via* diazo reaction. The representative bright field image in (f) shows fluorescent ZnO QDs in the respective assemblies. The optical microscope image presented in (i) exhibits the crystallisation of ultrasmall particles into supramolecular architectures. The synthetic methodology of the formation of nanoparticle assemblies at the interfaces is summarised in Scheme 1.

Typical scanning electron microscopy images of the representative hybrid assemblies formed at the *n*-hexane, dichloromethane, chloroform and toluene interfaces are shown in Fig. 2.

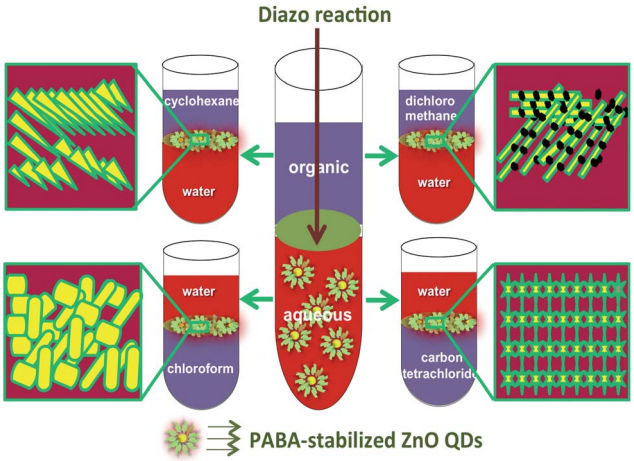

Scheme 1 Schematic presentation showing the formation of representative assemblies at the aqueous–organic interfaces.

It can be clearly observed that variation of the organic solvent of the immiscible liquid pairs results in morphological diversity with specific structural features. The composition of the hybrid assemblies formed at the water/toluene interface was determined from the EDX spectrum (shown in the inset) and confirm the presence of Zn elements in the composites.[21] The signals of C, O and Si elements come from the ZnO, diazotized product of PABA and the silicon wafer employed for the SEM measurement. Some closer views (images a–c) on the morphology of the assemblies at the water–*n*-hexane interface and microtomed SEM images

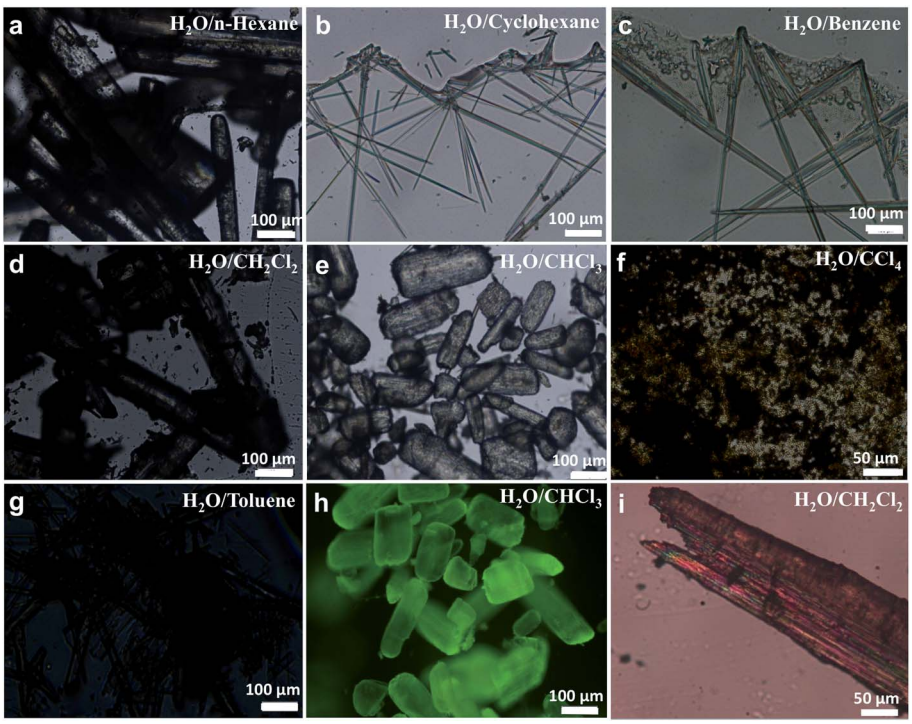

Fig. 1 (a–g) Dark field fluorescence microscopic images of the supramolecular assemblies of ZnO quantum dots in different solvents; (h) bright field image of the assembly formed at the water–chloroform interface and (i) optical microscope image in dichloromethane showing the assembling of quantum dots at one end.

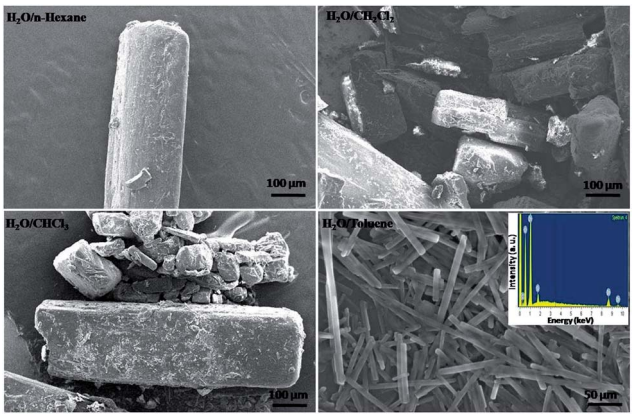

Fig. 2 Representative SEM images of the resulting hybrid assemblies formed at aqueous–organic interfaces. Inset shows the EDX spectrum of the hybrid assemblies formed at the water–toluene interface.

(image (d)) of the hybrid assemblies formed at the water–toluene interface are shown in Fig. 3. From the SEM images, it is evident that the ultrasmall particles are tightly packed in the assembly. Image (d) represents the cross-sectional SEM image showing the internal arrangement of the nanoparticles and indicating the solid interior of the supramolecular assemblies.[22]

Since ZnO QDs are fluorescent, the formation of the assembly could be followed by fluorescence spectroscopy (Fig. 4A). Both the spectra were measured in the solid state (λ_{ex} ~276 nm). The PABA-stabilised ZnO QDs show an UV emission band (λ_{em} ~337 nm) which is due to the direct band gap transition in the nanostructures.[23,24] Upon diazotisation, the emission peak shifts towards a longer wavelength in the visible range that can be attributed to the dominance of intrinsic defects which perturbs its band structure to form a discrete energy level within the bandgap. Therefore, it seems that the formation of superstructures controls the various aspects of the recombination process and favours the radiative transitions from the oxygen vacancies/trap levels in the bandgap to give a broad visible luminescence for the assemblies.[25] Inset shows the

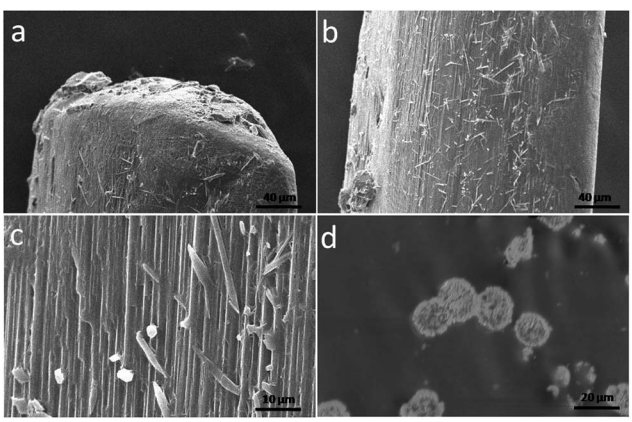

Fig. 3 SEM images (a) top view, (b) side view, (c) a closer look of the side view of the resulting hybrid assemblies formed at the water–*n*-hexane interface; and (d) microtomed SEM images of the hybrid assemblies formed at the water–toluene interface showing the solid interior.

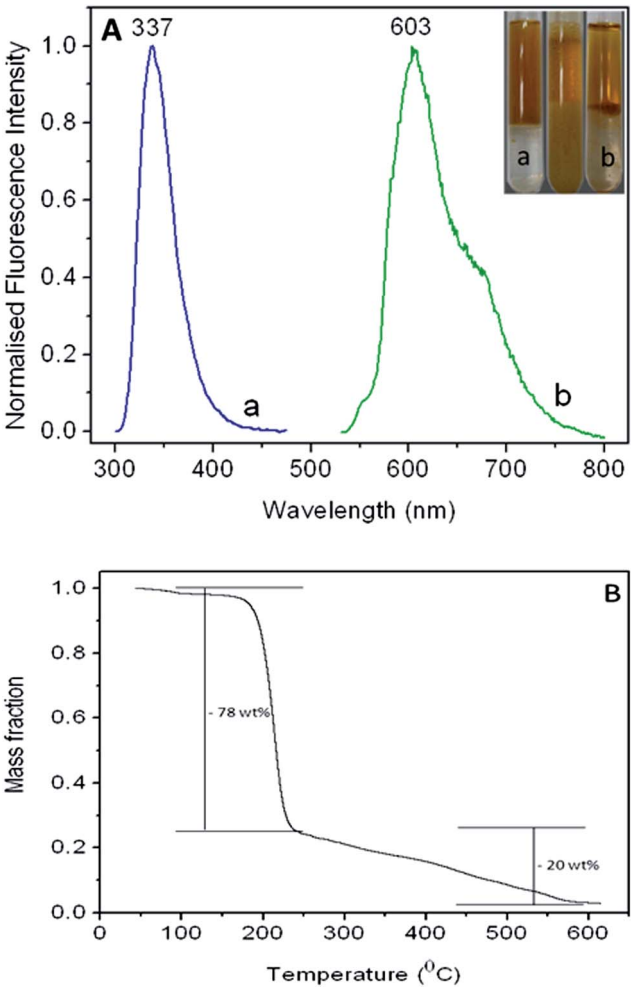

Fig. 4 (A) Fluorescence spectra of (a) PABA-stabilised ZnO nanoparticles and (b) after formation of assembly at water–CCl_4 interface. Inset shows the digital camera photograph of the formation of the assembly at the interface. (B) TGA curve of the hybrid assembly formed in chloroform.

digital camera photograph of the formation of the assembly at the liquid–liquid interface. An idea about the composition of the assembly has been obtained from TGA measurements. TGA measurement (Fig. 4B) of the as-dried powder sample of the assembly formed in chloroform shows two weight loss steps in the curve: 78 wt% loss corresponding to the desorption of water and organic solvent up to 200 °C, and a weight loss of 20 wt% over 200–800 °C as a result of the decomposition of arylamine compounds formed upon diazotisation in the composite. This means that 98 wt% loss of weight was observed up to 800 °C and only 2 wt% of the architecture is ZnO particles. This unusual weight loss, in the present experiment, is due to the fact that as the particle size is very small and correspondingly the overall surface area is very high, a large quantity of PABA molecules are involved for the stabilisation of the ZnO particles and subsequently, form the assembly upon diazotisation. Similar pattern in the TGA curve were also seen in the case of other solvents. These results suggest that organic molecules are, indeed, incorporated into the supramolecular assemblies.[26]

The successful 'diazo reaction' amongst the amine functionality of the PABA-stabilised ZnO QDs was confirmed by Fourier transform infrared spectroscopy (Fig. 5). Before diazotisation (trace a), for PABA-stabilised ZnO QDs, clear twin peaks are observed for primary amine functionalities ($-NH_2$) at 3406 cm^{-1} and 3300 cm^{-1}. After diazotisation (trace (b)), one single peak at 3362 cm^{-1} (in the range of amine) is observed indicating the presence of a secondary amine (–NH–) group and in addition, the appearance of a sharp strong peak at 1441 cm^{-1} confirms the presence of the –N=N– moiety.[27] The additional peak at about 3425 cm^{-1} arises due to the moisture adsorbed by the samples under atmospheric conditions. In trace (a), the peak at 1435 cm^{-1}, which is also present in trace (b) but it is overlapped with newly arise –N=N– peak at 1440 cm^{-1}, could be assigned to –C–H in plane bending vibrations.[28] It is, therefore, evident that –NH–N=N– linkage is formed upon diazotisation and subsequent arylamine formation[29] as shown in ESI 3.†

The X-ray diffraction pattern of the representative hybrid assemblies formed at the water–*n*-hexane interface is shown in Fig. 6A. The pattern in trace (a) is of weak reflections of PABA-stabilised ZnO nanoparticles. After diazotisation, strong reflections located in the small angle region reveal the polymerisation of the organic moiety as shown in trace (b). Other strong reflections in trace (b) could be indexed as pure hexagonal phase of Zn with a space group of C_{6v}^4 and cell constants a = 3.25 Å, and c = 5.21 Å (JCPDS card no.: 76-0704), which suggests that the product comprises ZnO nanocrystals with the wurtzite structure.[30] Fig. 6B shows the Raman spectrum of the assembly formed in *n*-hexane. The structure of ZnO belongs to the C_{6v}^4 symmetry group having two formula units per primitive cell with all the atoms occupying the C_{3v} sites, which predicts eight sets of zone centre optical phonons: two A_1, two E_1, two E_2 and two B_1 modes. Among these, A_1 and E_1 modes are polar and split into transverse (A_1T and E_1T) and longitudinal (A_1L and E_1L) phonons, all being Raman and infrared active; E_2 modes are non-polar consisting of two modes of low- and high-frequency (E_2L and E_2H) phonons and are only Raman active, and B_1 modes are infrared and Raman inactive (silent modes).[31] The main dominant sharp peak labeled as E_2 at 437 cm^{-1} is observed which is the characteristic of wurtzite hexagonal phase of ZnO. The peak at 300 cm^{-1} appears due to the silica substrate; other peaks attributable to 388 cm^{-1} as A_1T, 409 cm^{-1} as E_1T, 438 cm^{-1} as E_2H, 537 cm^{-1} as TO + TA(M) (transverse optical and transverse acoustic arising from zone boundary (M point)), 581 cm^{-1} E_1L, and 658 cm^{-1} as E_2L–B_1H respectively were observed as in the previous reports.[31]

A reasonable mechanism for the control of morphology of the inorganic–organic hybrid assemblies upon variation of the water-immiscible solvent of the aqueous–organic couple as confirmed by multiple control experiments could be enunciated as follows. It is, now, well established in the literature that a liquid–liquid interface is a non-homogeneous region having a thickness of the order of a few nanometers.[3] The interface between two immiscible liquids, thus, offers an important scaffold for the chemical manipulation and self-assembly of the nanocrystals.[32] When free PABA molecules are subjected to diazo reaction under similar reaction conditions, formation of no such assemblies are apparent at the interface indicating that

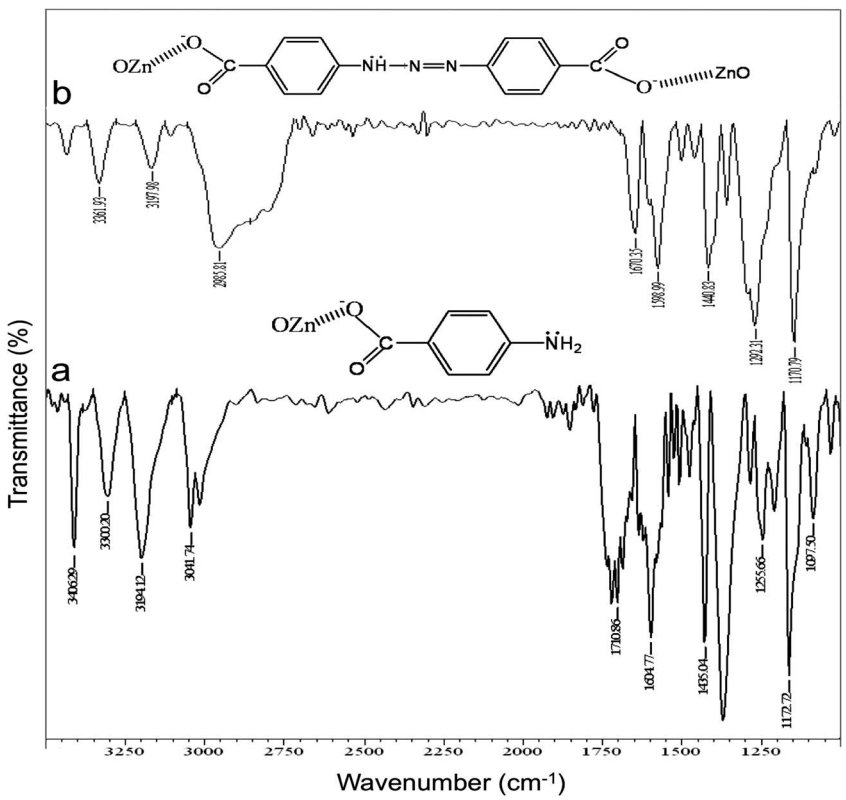

Fig. 5 FTIR spectra of (a) PABA-stabilised zinc oxide nanoparticles and (b) after formation of assembly at the water–cyclohexane interface.

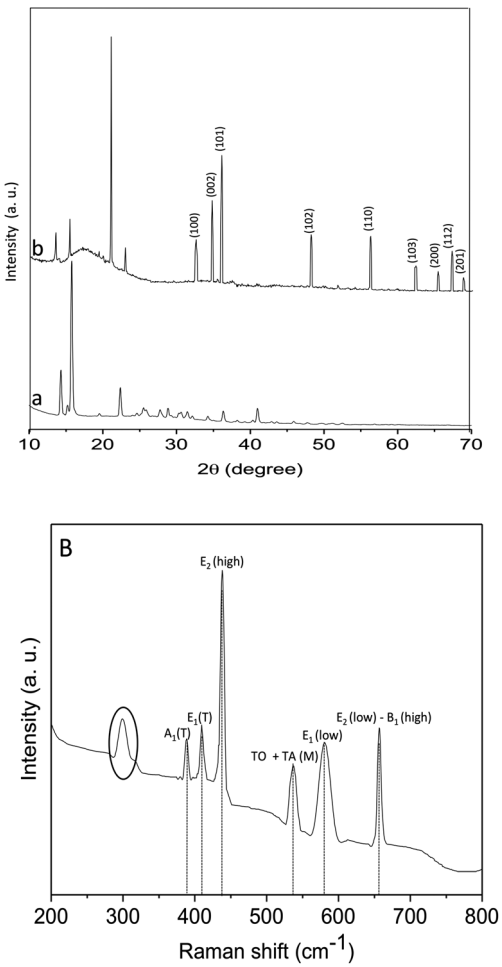

Fig. 6 (A) X-ray diffraction patterns of (a) PABA-stabilised ZnO and (b) after diazo reaction; (B) Raman spectra of the assembly formed in *n*-hexane.

PABA-stabilised ZnO QDs are indispensable for the formation of the assemblies. Upon shaking the nanoparticles in the presence of immiscible liquid pairs, without diazo reaction, phase separation occurs at the interface. In the absence of organic solvents, the ZnO particles upon diazotisation, escape out and creep on the wall of the test tube above the aqueous phase. No dissolution of the ZnO QDs is seen under the diazo reaction condition. Therefore, it is manifested that while the liquid–liquid interface offers a viable platform, the diazo reaction acts as the main architect in maneuvering the inorganic–organic hybrid assemblies. Thus, the observed assembly is the result of specific PABA–PABA interactions; the importance of the diazo reaction and subsequent arylamine formation[29] enable effective interparticle interaction in harnessing the assemblies. The interfacial tension at the water–organic interface renders a versatile platform for assembly of the particles, which, in turn, generates variable morphology through oriented attachment. Moreover, it is observed that the hybrid assemblies could not be achieved in the presence of other water-immiscible solvents, like, DMF, DMSO, THF, acetonitrile *etc.* Therefore, it could be conceived that the observed ordering is the result of the interplay of two or more of the physical properties providing the environment required to achieve unprecedented morphologies of nanoparticle assemblies.[32]

As a direct and large-band-gap material, ZnO has attracted immense interest for a wide range of devices, including transparent thin-film transistors, photodetectors, light-emitting diodes and laser diodes that operate in the blue and ultraviolet region of the spectrum.[33] The advantages associated with ZnO include higher breakdown voltages, ability to sustain large electric fields, lower noise generation, and high temperature and high-power operation.[34–36] On the other hand, PABA molecules attached onto the ZnO surface, upon diazotisation, form a polyaniline-like network that renders important electrical conductivity. The dc electrical conductivities of the inorganic–organic hybrid assemblies as a function of temperature (283–373 K) were measured by multimeter. Electron transport in a thin film of each assembly was measured using an electrode geometry in which the conductivity was measured between two contacts which are separated by a narrow gap bridged by the material of interest. Fig. 7 shows the profile of the variation of $\ln(\sigma)$ as a function of $1/T$ (where σ is the measured electrical conductivity of the dried assemblies in mho and T the absolute temperature). The electrical conductivity at first increases, reaches an optimum, and then becomes almost constant after a particular temperature. However, it is noted that the electrical conductivity in different morphologies does not vary as appreciably as different morphologies that may arise from different growth directions or internal strains.[16] Thus, the interdigitation of semiconducting ZnO nanoparticles with polymeric arylamine networks could be exploited to yield good conducting materials.

The photoluminescence spectra of the dried supramolecular assemblies with an excitation wavelength of 276 nm are shown in Fig. 8. All the spectra were measured in the solid state. It is seen that the emission spectra of all the supramolecular assemblies are red shifted compared to the individual ZnO nanoparticles as seen in Fig. 4A. Moreover, the salient feature of physical significance is that the hybrid assemblies formed at the aqueous–organic interface exhibit distinctly different emission profiles in the superstructures. This red shifted emission could be attributed to the formation of superstructures that controls

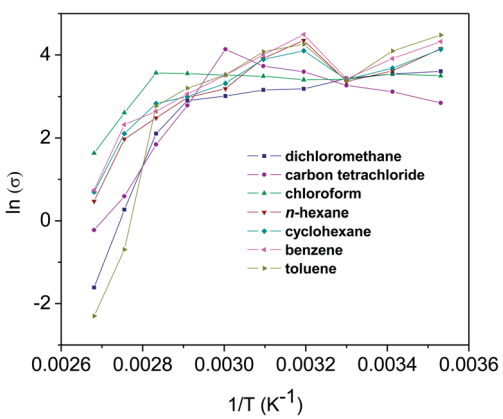

Fig. 7 Variation of electrical conductivity of the dried supramolecular assemblies as a function of temperature.

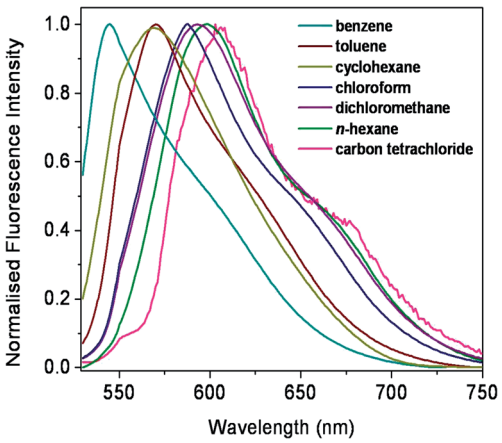

Fig. 8 Photoluminescence spectra of the dried supramolecular assemblies at room temperature.

the various aspects of the recombination process and favours radiative transitions from the oxygen vacancies/trap levels in the bandgap to give a broad visible luminescence for the assemblies.[25] Therefore, the photoluminescence properties of hybrid assemblies of ZnO QDs could be exploited in the fabrication of optoelectronic devices.

4. Conclusion

In summary, liquid–liquid interfaces offer viable platforms for designing functional supramolecular assemblies of ZnO quantum dots into micrometer to millimeter-sized objects by diazo reaction. The ease and specificity of the diazo reaction and subsequent arylamine formation directs the self-assembly of the inorganic particles and controls their spatial arrangement to induce unique morphology in the hybrid assemblies. Morphological versatility could be achieved by judicious selection of immiscible liquid pair, careful manipulation of the stabilising ligand shell and exploring feasible cross-linking strategies for designing hierarchical assemblies with newer functionalities. Finally, by proper choice of the constituent nanoparticles, such assemblies could be envisaged in various magnetic, fluorescent and photonic materials.

Acknowledgements

We gratefully acknowledge financial support from DST, New Dehli (Project No.: SR/FT/CS-68/2010). We are thankful to Dr. Nikhil R. Jana, IACS, Kolkata for providing microscopic facilities and Dr. Achintya Ray, Bose Institute, Kolkata for Raman measurements.

References

1 D. M. Vriezema, M. C. Aragones, J. A. A. W. Elemans, J. J. L. M. Cornelissen, A. E. Rowan and R. J. M. Nolte, *Chem. Rev.*, 2005, **105**, 1445–1489.
2 W. H. Binder, *Angew. Chem., Int. Ed.*, 2005, **44**, 5172–5175.
3 A. Böker, J. He, T. Emrick and T. P. Russell, *Soft Matter*, 2007, **3**, 1231–1248.
4 Y. Lin, H. Skaff, A. Böker, A. D. Dinsmore, T. Emrick and T. P. Russell, *J. Am. Chem. Soc.*, 2003, **125**, 12690–12691.
5 H. Duan, D. Wang, D. G. Kurth and H. Möhwald, *Angew. Chem., Int. Ed.*, 2004, **43**, 5639–5642.
6 Z. Niu, J. He, T. P. Russel and Q. Wang, *Angew. Chem., Int. Ed.*, 2010, **49**, 10052–10066.
7 H. Gu, Z. Yang, J. Gao, C. K. Chang and B. Xu, *J. Am. Chem. Soc.*, 2005, **127**, 34–35.
8 A. H. Gröschel, A. Walther, T. I. Löbling, J. Schmelz, A. Hanisch, H. Schmalz and A. H. E. Müller, *J. Am. Chem. Soc.*, 2012, **134**, 13850–13860.
9 W. Lu and C. M. Lieber, *J. Phys. D: Appl. Phys.*, 2006, **39**, R387–R406.
10 Y. Gu, I. L. Kuskovsky, M. Yin, S. O'Brien and G. F. Neumark, *Appl. Phys. Lett.*, 2004, **85**, 3833–3835.
11 Y. R. Ryu, S. Zhu, J. D. Budai, H. R. Chandrasekhar, P. F. Miceli and H. W. White, *J. Appl. Phys.*, 2000, **88**, 201.
12 P. Nunes, B. Fernandes, E. Fortunato, P. Vilarinho and R. Martins, *Thin Solid Films*, 1999, **337**, 176–179.
13 L. Wang and N. C. Giles, *J. Appl. Phys.*, 2003, **94**, 973–975.
14 *ZnO Bulk, Thin Films, and Nanostructures*, ed. C. Jagadish and S. Pearton, Elsevier, 2006.
15 D. C. Look, *Mater. Sci. Eng., B*, 2001, **80**, 383–387.
16 A. P. Alivisatos, *Science*, 1996, **271**, 933–937.
17 Z. L. Wang, *J. Phys.: Condens. Matter*, 2004, **16**, R829–R858.
18 T.-M. Shang, J. -H. Sun, Q. -F. Zhou and M. -Y. Guan, *Cryst. Res. Technol.*, 2007, **42**, 1002–1006.
19 G. M. Whitesides and M. Boncheva, *Proc. Natl. Acad. Sci. U. S. A.*, 2002, **99**, 4769–4774.
20 C. Pacholski, A. Kornowski and H. Weller, *Angew. Chem., Int. Ed.*, 2002, **41**, 1188–1191.
21 H. Wang, A. J. Patil, K. Liu, S. Petrov, S. Mann, M. A. Winnik and I. Manners, *Adv. Mater.*, 2009, **21**, 1805–1808.
22 S. Stankovich, D. A. Dikin, G. H. B. Dommett, K. M. Kohlhaas, E. J. Zimney, E. A. Stach, R. D. Piner, S. B. T. Nguyen and R. S. Ruoff, *Nature*, 2006, **442**, 282–286.
23 H. Zhou, H. Alves, D. M. Hofman, W. Kriegseis, B. K. Meyer, G. Kaczmarczyk and A. Hoffmann, *Appl. Phys. Lett.*, 2002, **80**, 210–212.
24 I. Shalish, H. Temkin and V. Narayanamurti, *Phys. Rev. B: Condens. Matter Mater. Phys.*, 2004, **69**, 245401–245404.
25 R. J. Mendelsberg, M. W. Allen, S. M. Durbin and R. J. Reeves, *Phys. Rev. B*, 2011, **83**, 205202–205209.
26 H.-P. Cong and S.-H. Yu, *Adv. Funct. Mater.*, 2007, **17**, 1814–1820.
27 P. Griffiths, J. A. de Hasseth, in *Fourier Transform Infrared Spectroscopy*, 2nd edn, Wiley Interscience, Hoboken, New Jersey, 2007.
28 N. Sundaraganesan, H. Umamaheswari, B. D. Joshua, C. Meganathan and M. Ramalingam, *J. Mol. Struct.: THEOCHEM*, 2008, **850**, 84–93.

29 P. Sykes, in *A Guidebook to Mechanism in Organic Chemistry*, 6th edn, Longman, London, 1986.
30 M. Goano, F. Bertazzi, M. Penna and E. Bellotti, *J. Appl. Phys.*, 2007, **102**, 083709–083719.
31 C. A. Arguello, D. L. Rousseau and S. P. Porto, *Phys. Rev.*, 1969, **181**, 1351–1363.
32 D. Nykypanchuk, M. M. Maye, D. van der Lelie and O. Gang, *Nature*, 2008, **451**, 549–552.
33 Ü. Özgur, Y. I. Alivov, C. Liu, A. Teke, M. A. Reshchikov, F. Doğan, V. Avrutin, S.-J. Cho and H. Morkoç, *J. Appl. Phys.*, 2005, **98**, 41301–42103.
34 J. D. Albrecht, P. P. Ruden, S. Limpijumnong, W. R. L. Lambrecht and K. F. Brennan, *J. Appl. Phys.*, 1991, **86**, 6864–6867.
35 P. H. Miller Jr, *Phys. Rev.*, 1941, **60**, 890–895.
36 A. Janotti and C. G. van de Walle, *Rep. Prog. Phys.*, 2009, **72**, 126501–126529.

Nanoparticle-Decorated Ultrathin Membrane at the Water-Toluene Interface

Authors: Ghosh, Sujit Kumar; Ali, Mohammed; Garain, Samiran

Source: Advanced Science, Engineering and Medicine (/content/asp/asem), Volume 6, Number 3, March 2014, pp. 333-337(5)

Publisher: American Scientific Publishers (/content/asp)

< previous article (/content/asp/asem/2014/00000006/00000003/art00013) |
view table of contents (/content/asp/asem/2014/00000006/00000003) |
next article > (/content/asp/asem/2014/00000006/00000003/art00015)
☆ ADD TO FAVOURITES

Abstract:

A simple and facile route is presented to fabricate robust membrane based on the interfacial self-assembly of 11-mercaptoundecanoic acid-covered gold nanoparticles and cetylpyridinium chloride in the presence of a weak base at the water-toluene interface. Observation of the interfacial self-assembly by microscopic techniques demonstrates the formation of nanoparticle-decorated ultrathin membrane composed of close-packed nanoparticles with liquid-like ordering. The ion-pair formation between 11-mercaptoundecanoic acid-covered gold nanoparticles and cetylpyridinium chloride in the presence of a weak base has been confirmed by UV-Vis and FTIR spectroscopy. The formation of structurally intact membrane at the interface enables the encapsulation of selective water-soluble dye molecules exhibiting permeability for real-time applications.

Keywords: INTERFACE (/search?option1=tka&value1=INTERFACE); MEMBRANE (/search?option1=tka&value1=MEMBRANE); NANOPARTICLES (/search?option1=tka&value1=NANOPARTICLES); PERMEABILITY (/search?option1=tka&value1=PERMEABILITY); SELF-ASSEMBLY (/search?option1=tka&value1=SELF-ASSEMBLY)

Document Type: Research Article

DOI: http://dx.doi.org/10.1166/asem.2014.1484 (http://dx.doi.org/10.1166/asem.2014.1484)

Publication date: March 1, 2014

More about this publication?
Related content